



Estimation of Time Scales in Unsteady Flows in a Turbomachinery Rig

Jacques Lewalle
Syracuse University, Syracuse, New York

David E. Ashpis
Glenn Research Center, Cleveland, Ohio

The NASA STI Program Office . . . in Profile

Since its founding, NASA has been dedicated to the advancement of aeronautics and space science. The NASA Scientific and Technical Information (STI) Program Office plays a key part in helping NASA maintain this important role.

The NASA STI Program Office is operated by Langley Research Center, the Lead Center for NASA's scientific and technical information. The NASA STI Program Office provides access to the NASA STI Database, the largest collection of aeronautical and space science STI in the world. The Program Office is also NASA's institutional mechanism for disseminating the results of its research and development activities. These results are published by NASA in the NASA STI Report Series, which includes the following report types:

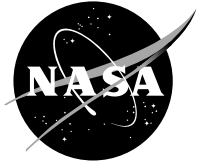
- **TECHNICAL PUBLICATION.** Reports of completed research or a major significant phase of research that present the results of NASA programs and include extensive data or theoretical analysis. Includes compilations of significant scientific and technical data and information deemed to be of continuing reference value. NASA's counterpart of peer-reviewed formal professional papers but has less stringent limitations on manuscript length and extent of graphic presentations.
- **TECHNICAL MEMORANDUM.** Scientific and technical findings that are preliminary or of specialized interest, e.g., quick release reports, working papers, and bibliographies that contain minimal annotation. Does not contain extensive analysis.
- **CONTRACTOR REPORT.** Scientific and technical findings by NASA-sponsored contractors and grantees.

- **CONFERENCE PUBLICATION.** Collected papers from scientific and technical conferences, symposia, seminars, or other meetings sponsored or cosponsored by NASA.
- **SPECIAL PUBLICATION.** Scientific, technical, or historical information from NASA programs, projects, and missions, often concerned with subjects having substantial public interest.
- **TECHNICAL TRANSLATION.** English-language translations of foreign scientific and technical material pertinent to NASA's mission.

Specialized services that complement the STI Program Office's diverse offerings include creating custom thesauri, building customized databases, organizing and publishing research results . . . even providing videos.

For more information about the NASA STI Program Office, see the following:

- Access the NASA STI Program Home Page at <http://www.sti.nasa.gov>
- E-mail your question via the Internet to help@sti.nasa.gov
- Fax your question to the NASA Access Help Desk at 301-621-0134
- Telephone the NASA Access Help Desk at 301-621-0390
- Write to:
NASA Access Help Desk
NASA Center for AeroSpace Information
7121 Standard Drive
Hanover, MD 21076



Estimation of Time Scales in Unsteady Flows in a Turbomachinery Rig

Jacques Lewalle
Syracuse University, Syracuse, New York

David E. Ashpis
Glenn Research Center, Cleveland, Ohio

National Aeronautics and
Space Administration

Glenn Research Center

Acknowledgments

The data for this work was provided by Dr. David Halstead and Dr. David Wisler from General Electric Aircraft Engines. Their assistance and cooperation are greatly appreciated.

Trade names or manufacturers' names are used in this report for identification only. This usage does not constitute an official endorsement, either expressed or implied, by the National Aeronautics and Space Administration.

Available from

NASA Center for Aerospace Information
7121 Standard Drive
Hanover, MD 21076

National Technical Information Service
5285 Port Royal Road
Springfield, VA 22100

Available electronically at <http://gltrs.grc.nasa.gov>

Estimation of Time Scales in Unsteady Flows in a Turbomachinery Rig

Jacques Lewalle

Department of Mechanical, Aerospace and Manufacturing
Engineering
Syracuse University
and

David E. Ashpis
NASA Glenn Research Center

Abstract

Time scales in turbulent and transitional flow provide a link between experimental data and modeling, both in terms of physical content and for quantitative assessment. The problem of interest here is the definition of time scales in an unsteady flow. Using representative samples of data from GEAE low pressure turbine experiment in low speed research turbine facility with wake-induced transition, we document several methods to extract dominant frequencies, and compare the results. We show that conventional methods of time scale evaluation (based on autocorrelation functions and on Fourier spectra) and wavelet-based methods provide similar information when applied to stationary signals. We also show the greater flexibility of the wavelet-based methods when dealing with intermittent or strongly modulated data, as are encountered in transitioning boundary layers and in flows with unsteady forcing associated with wake passing. We define phase-averaged dominant frequencies that characterize the turbulence associated with freestream conditions and with the passing wakes downstream of a rotor. The relevance of these results for modeling is discussed in the paper.

1 Introduction

Dominant turbulent time scales characterize important physics of turbulence, and are featured prominently in models applicable to turbomachinery flows: the ratio κ/ε characterizes large eddies and is ubiquitous in the modeled expressions of the transport, production and destruction terms. The problem is that conventional methods (based on autocorrelation functions and Fourier analysis) are ill-suited to the treatment of unsteady data. In this paper, we compare the time scales obtained from conventional and wavelet tools, and illustrate unique capabilities of the wavelet algorithms downstream of a rotor.

Three goals were addressed in the process.

1. A quantitative comparison of integral scales and most-energetic scales, based on conventional methods applicable to stationary signals (use of autocorrelation functions and Fourier spectra), shows that the two scales are not very different. This allows us to focus on most-energetic scales while allowing the results to be converted to the integral-scales favored by modelers.
2. Then, we show that wavelet-based methods present an alternative to the Fourier spectra, with excellent quantitative agreement. Thus, the integral scale information can be obtained from wavelet-based results.
3. Finally, we use the greater flexibility of the wavelet methods to extend the measurement of dominant time-scales to the unsteady environment of embedded stages. The flow characterization obtained in this manner may be compared with unsteady numerical results.

1.1 Time scales and modeling

Let us define modeling as the construction of systems simpler than the complex reality. The selection of relevant physics at the exclusion of unessential features is at the core of any scientific or engineering model, and sets the limits of its applicability. Indeed we might think of the compressible Navier-Stokes equations as ‘reality’, but the depiction of the fluid as a continuum is certainly a model, with known limits of accuracy. Thus, it is proper to envision a hierarchy of models of reality, with high-level models providing a point of reference in terms of accessibility and accuracy of the solutions. Lower level models are obtained by ignoring some terms, or by using simpler alternatives for analytically-difficult terms; explicit reference to the higher-level model may even be eliminated in some cases.

An engineering model will be conceived and evaluated based on considerations of

- physical content: qualitative or quantitative model predictions can be expected only if the relevant dynamics are included in some form. It would make little sense to ignore turbulent transport in studying flow through turbomachinery, whereas the same assumption is acceptable in the context of homogeneous turbulence.
- analytical form: with no known general form of the transport terms in averaged equations for turbulent flows, eddy-viscosity models are frequently used.
- quantitative parameter tuning: by adjusting model constants, model predictions can have quantitative value to the engineer.

The material presented in this report might affect physical content as well as quantitative adjustments in turbomachinery flow modeling.

The selection of physical content in a model is usually based, more or less explicitly, on scale considerations. Molecular and sub-molecular dynamics are not considered essential in describing flows over scales much larger than the mean-free-path; climatic drift is not essential in updating weather predictions for the next few days; and so forth. In some circumstances, the energy spectrum characteristic of the phenomenon will exhibit gaps, which effectively isolate some spectral ranges and allow us to study them in isolation; in other cases such as turbulence, broad-band spectral activity dictates a more cautious approach to model construction.

In this introduction, we will use length- or time-scales indifferently; the data analysis will focus on the more directly accessible time scales. Based on the features of a typical power spectrum of a turbulent flow as on Fig.1¹, one can identify several scales: starting from low-frequencies,

1. the point, at approximately 1kHz , where the energy content starts decreasing is distinctive (macroscale),
2. as is the range of scales, around 4kHz , in which power-law behavior is exhibited,
3. as is the point, approximately 8kHz , at which the spectrum tails down (microscale or limit of resolution).

Appropriate definitions help us pinpoint these scales: integral scales, Taylor and Kolmogorov microscales, etc. The interest of these scales in modeling is that they are representative of certain dynamical effects at the exclusion of others, in spite of the absence of a spectral gap. For instance,

¹it is immaterial for this illustration that the high frequency drop-off is actually due to low-pass filtering rather than to actual viscous dissipation

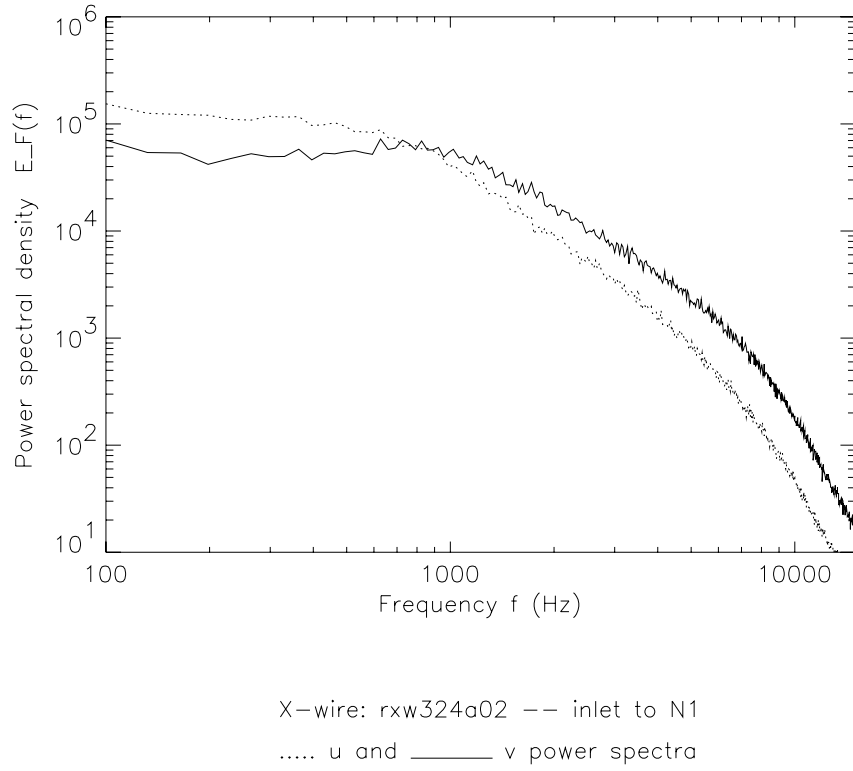


Figure 1: *Longitudinal (dotted line) and transverse (solid line) power spectral density at inlet of nozzle 1.*

1. the Kolmogorov microscale is characteristic of the viscous dissipation of energy, and (at large Reynolds numbers) contains very little energy and accomplishes very little transport or mixing.
2. the Taylor microscale is representative of the absence of either viscous or transport effects: from the equations of motion, only unsteady inertia effects (convection/pressure/spectral transfer) remain.
3. the macroscales can be defined as either integral scales or as energy-containing scales: they are representative of large eddies that accomplish much of the mixing in the turbulent flow, and of the production of turbulence energy, in isolation from significant viscous effects. The remainder of this paper will focus on the macroscales.

This scale separation of the various dynamical terms is at the basis of much turbulence modeling. For example, Kolmogorov's equilibrium range model (small scale) combines inertial and viscous effects. Closer to the subject of this report, in modeling the transport terms in a turbulent flow, macroscale parameters should be used. Using viscous scaling for turbulent transport would generally be regarded as bad modeling on account of the inappropriate physical content. Thus, a suitable understanding of the turbulent macroscales and their quantitative evaluation are at the core of any model of turbulent transport.

Time scales are particularly indicated in the context of this project because of the following reasons:

- the data was collected as time series, so that characteristic frequencies are more natural than a corresponding wavenumber – the conversion between the two makes use of Taylor’s Hypothesis.
- it is generally accepted (see e.g. Tennekes & Lumley, p.70) that the ratio of time scales between two phenomena is a measure of how well correlated they are and of how effectively they exchange energy. For example, small eddies behave independently of the large scale turbulence; a process is adiabatic if it is fast relative to applicable time scales of energy transfer; etc. Thus, quantitative evaluations of time scales will provide a measure of physical interactions within the flow.
- most turbulence models (e.g. 2-equation models) provide ready access to large-eddy time-scales, in the form of κ/ε found in the construction of transport, production and destruction terms.

1.2 The data

In this study, we focus on the time-scales of anemometry data, in an attempt to identify sensitive algorithms capable of characterizing the physics of transitioning flows subject to rapid straining and unsteady freestream turbulence. The times scales are one channel by which experimental information is normally reflected in model results, and we expand the applicability of the idea to unsteady flows. The data is from an experiment conducted by Dr. David Halstead at GE Aircraft Engines (GEAE). The experiment was conducted at GEAE Low Speed Research Turbine rig on a two-stage low-pressure turbine. The configuration is shown in Fig. 2. Halstead took measurements with X hot-film probe at the inlet and exit of each blade row, with hot-wire probe in the boundary layers of the first and second stage nozzles, and with hot-film arrays surface-mounted on the second stage nozzle and rotor. The complete data set is the object of extensive analysis presented by Halstead et al. [4, 5]. The work presented in this report is limited to representative X-probe data taken at the inlet and the exit of the first stage Nozzle and Rotor, designated as N1 and R1, respectively. Work utilizing quasi-shear stress data from the surface hot-film arrays was performed by Lewalle [12]. It is expected that the methodology and data processing presented here will lead to further method development and extensive data analysis that will advance modeling of unsteady flows in turbomachinery.

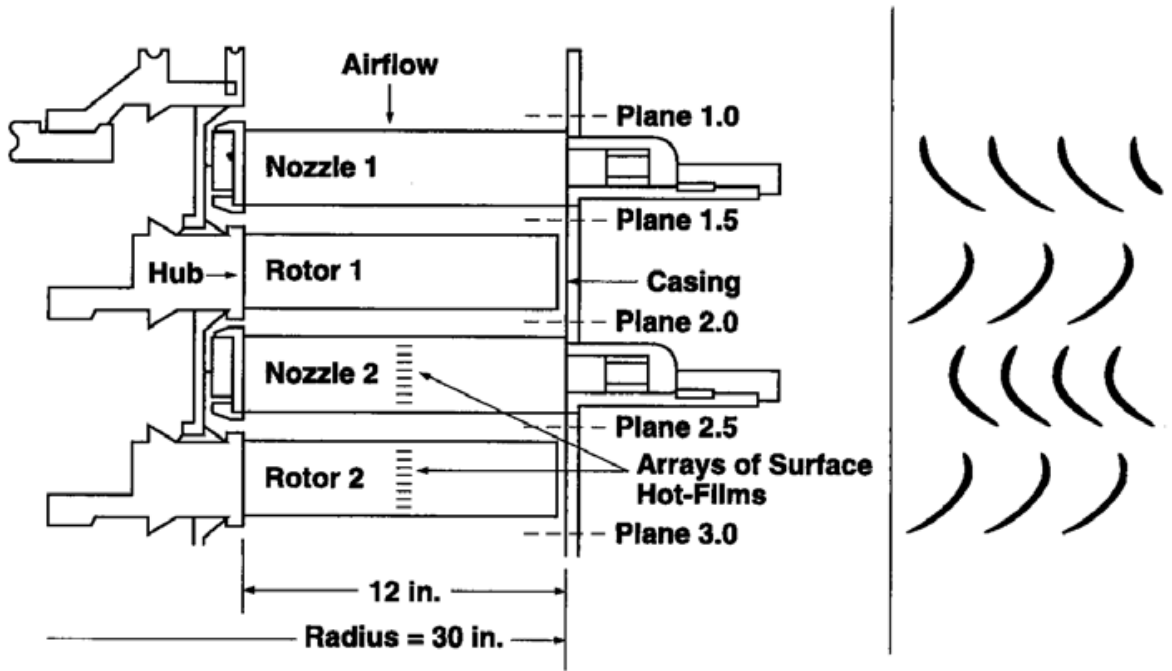


Figure 2: *Schematic of the facility*

1.2.1 Inlet conditions

At the inlet, unspecified ambient turbulence is present. On Fig. 3, we show an instantaneous trace, an ensemble average, the fluctuation around that average, and the skew at the N1 inlet. There is no appreciable periodic component of the incoming turbulence. As a result, the ensemble mean velocity reflects mostly the random fluctuations of the incoming flow, with an rms value presumably decreasing as the square root of the number of traces in the ensemble (Mean Value Theorem). Indeed we see that the rms of the ensemble mean is smaller than the rms of each trace by one order of magnitude. We will study the fluctuations around this mean.

1.2.2 Rotor exit conditions

On Fig. 4, we show an instantaneous trace, an ensemble average, the fluctuation around that average, and the skew. In contrast to the N1 inlet data, a strong periodic component can be identified on the raw data, and the ensemble mean shows strong, smooth periodicity with rms comparable to that of the raw signals. Minor variations from period to period in the ensemble mean reflect the turbulent fluctuations, which have a similar rms.

The ensemble mean velocity components were subtracted from the processed traces, using the formulae listed in Halstead [5]. This enables the ‘random’ turbulence to stand out from the periodicity of the wake shedding from R1. Then we

N1 rxw324a02 trace #1 Vx
raw Vx/ens av/Vx_prime/skew

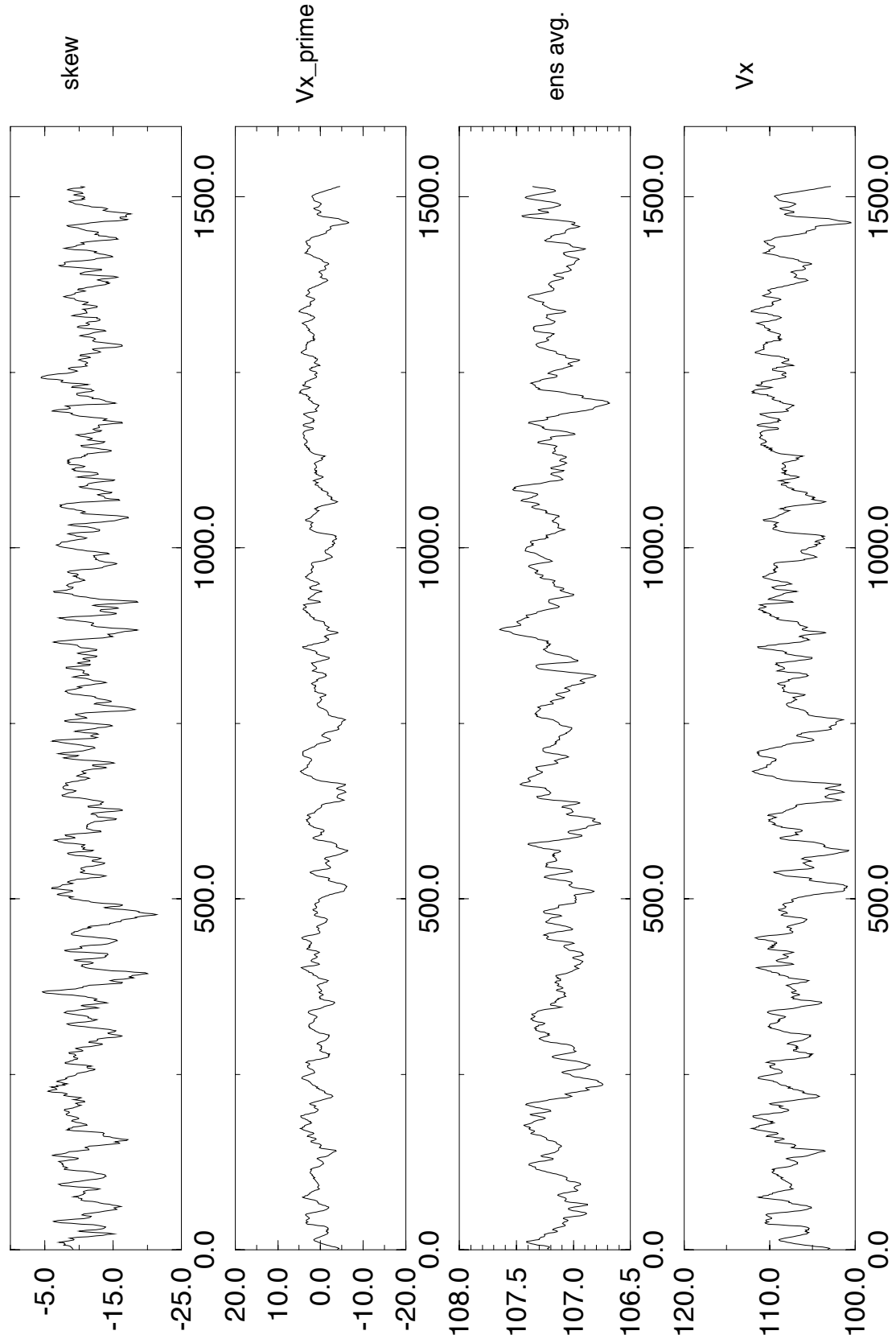


Figure 3: Streamwise velocity at the N1 inlet. From bottom to top: raw data, ensemble average (300 traces), fluctuation around the average, and skew.

N2 rxw324c04 trace #1 Vx
raw Vx/ens av/Vx_prime/skew

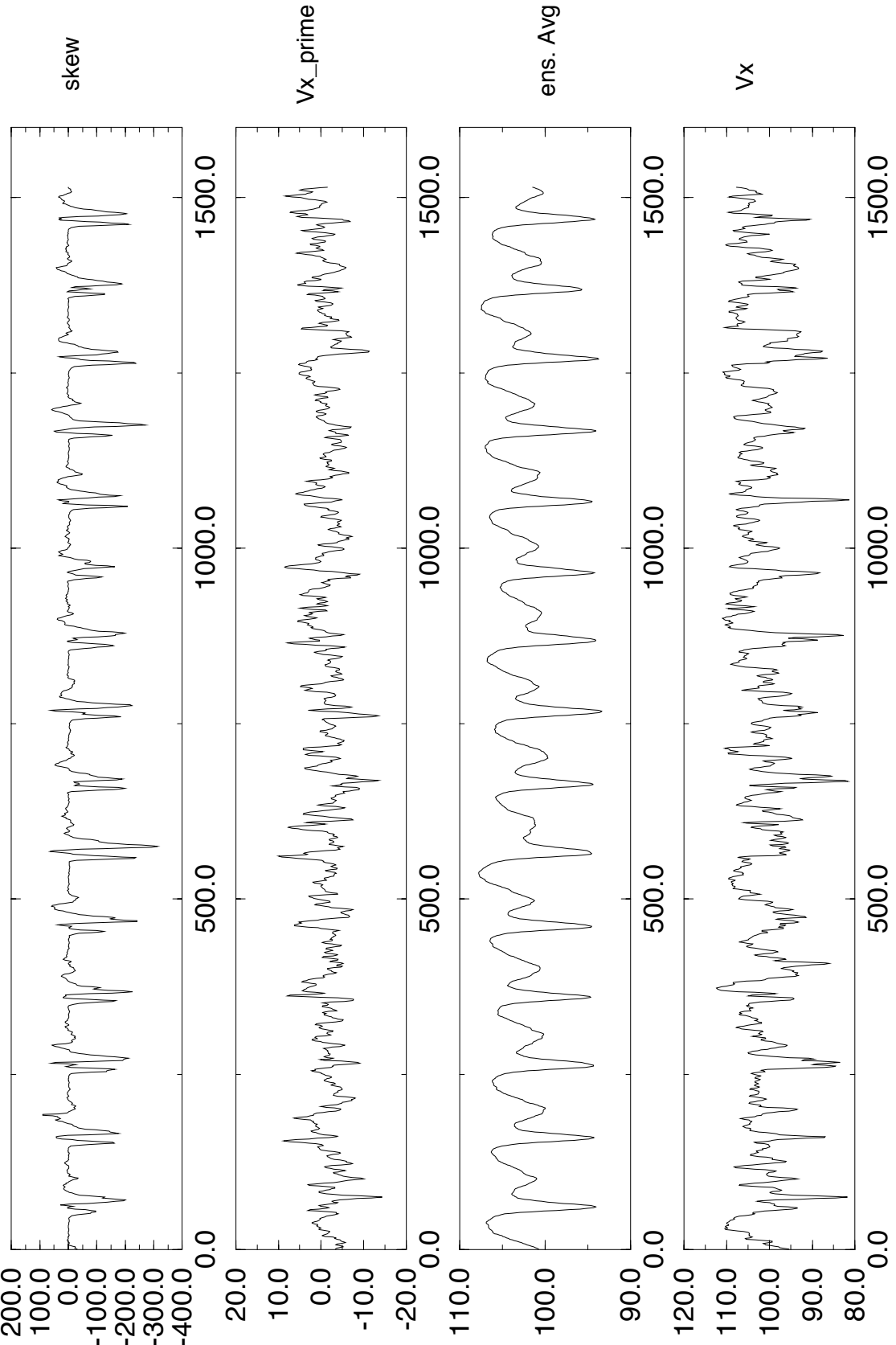


Figure 4: Streamwise velocity at the R1 exit. From bottom to top: raw data, ensemble average (300 traces), fluctuation around the average, and skew.

reproduced the statistics provided by Halstead, as a test of integrity of the processed data.

1.3 Overview

We proceeded with the calculation of several time scales from this data.

- calculation of the integral time scales, obtained by integration of the autocorrelation functions for the streamwise and transverse velocity components.
- calculation of the integral time scale from the zero-frequency estimate of the 1-dimensional power spectrum
- identification of the most-energetic scales from the Fourier power spectral density.
- identification of the most-active transporting scales from the Fourier cross-spectral density.
- identification of the most-energetic scales from the Morlet wavelet mean power spectrum.
- identification of the most-energetic scales from the Mexhat wavelet mean power spectrum
- identification of the most-active scales from the Mexhat Reynolds stress decomposition

Detailed presentation of these methods can be found in Hinze [7], Lewalle and Ashpis [11], and other references itemized in the Appendices. We compare and interpret the results as follows:

- at the inlet section, we tabulate the various statistics and note differences. We compare our results to classical isotropic-turbulence relations between integral scales and energy spectra [7]. This establishes the validity of the statistics for parameterization and characterization purposes.
- at the embedded station, we confirm that mean properties can be calculated by any of the same methods, and note that the mean statistics are rather unsatisfactory as descriptors of the complexity of the flow.
- the flexibility of wavelet spectra in relation with conditional sampling is illustrated with the construction of phase-dependent time scales. The variations in dominant turbulent scales during one period of wake-passing are mapped and discussed.

2 Method Validation on Stationary Data

We first document the time scales for stationary turbulence at the entrance to the first rotor (N1). The purpose is to show that similar results are obtained from integral time scales, dominant scales of the Fourier spectrum, and dominant wavelet scales. Unsteady data at the rotor exit (R1) will be treated in the next Section.

For brevity of the presentation, only essential formulae will be listed in this section. Details of implementation, differences between continuous and discrete formulations, and specifics relating to factors of 2π in the formulae, are listed in Appendix 1 for reference.

2.1 Integral time scales

Let us focus first on one velocity signal, say $u(t)$. Its standard deviation is measured by u' :

$$u'^2 = \lim_{T \rightarrow \infty} \frac{1}{2T} \int_{-T}^T |u(t)|^2 dt. \quad (1)$$

The longitudinal autocorrelation function for a stationary signal $u(t)$ is defined as

$$u'^2 f_u(t) = \overline{u(\tau)u(t+\tau)} \quad (2)$$

The autocorrelation functions measure the gradual loss of correlation as the time lag between measurements of the given component u increases. Analytical and experimental properties of these functions can be found in standard references [7]. For diagnostic purposes, it is convenient to summarize the information about the drop-off by a single number: the longitudinal integral time scale is defined as

$$T_{u,int} = \int_0^\infty f_u(t) dt, \quad (3)$$

In addition to the longitudinal autocorrelation function (Eq. 2) and integral time scale (Eq. 3), we define the transverse autocorrelation function

$$v'^2 g_v(t) = \overline{v(\tau)v(t+\tau)} \quad (4)$$

and transverse integral scale

$$T_{v,int} = \int_0^\infty g_v(t) dt. \quad (5)$$

Both autocorrelations are shown on Fig. 5. The correspondence between experimental results and model parameters is normally based on these integral scales. Integral scales are clearly defined, can be computed rapidly, and capture the ‘size’ of the large

(energy-containing) eddies. The natural time scale occurring in relation to these large eddies (a measure of eddy turnover time) in κ - ε models is the integral time scale

$$T_{u,int} = \frac{\kappa}{\varepsilon} \quad (6)$$

(see e.g. Wilcox, p.90-92), and all model constants are adjusted accordingly. The values can be converted to integral length scales using Taylor's Hypothesis under a convection velocity U :

$$\Lambda_f = UT_{u,int} \quad (7)$$

To make comparisons possible with results from later Sections, we had to choose between time scales or frequencies, and settled on the latter. The frequencies corresponding to the time scales above were calculated as

$$f_{u,int} = \frac{1}{2\pi T_{u,int}} = 0.606 \text{ kHz} \quad (8)$$

(respectively)

$$f_{v,int} = \frac{1}{2\pi T_{v,int}} = 1.106 \text{ kHz}. \quad (9)$$

We note that the approximate factor 2 between these two scales agrees with the theoretical relation between the longitudinal and transverse integral scales (Hinze [7], Eqs. 3-74 and 3-75) for isotropic turbulence.

Practically, the computation of the autocorrelation function is very time consuming. Furthermore the slow convergence of the function for large times makes its numerical integration rather inaccurate. For these reasons, an alternative definition based on the Fourier spectrum E_F (see Fig. 1) is generally preferred. It is easy to show (e.g. Hinze [7], p65) that the integral scale defined above can be calculated from the formula

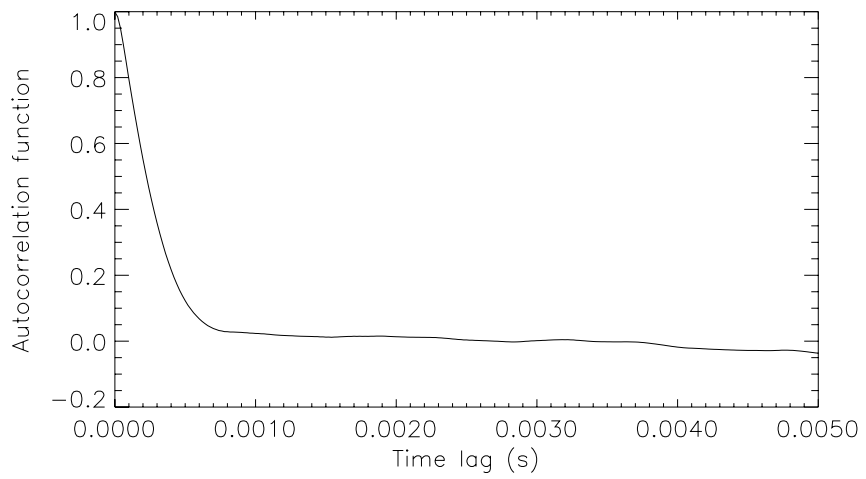
$$T_{u,int} = \frac{E_F(0)}{4u'^2} \quad (10)$$

The convergence problem for the autocorrelation function now takes the form of inaccuracies in the calculation of the low-frequency part of the spectrum. However, as the energy density is constant in this region of the spectrum, extrapolation of any well-converged part of the spectrum to lower frequencies gives reliable estimates of $E_F(0)$. Thanks to the use of FFT's, the integral scales can be calculated very efficiently. These observations combine to make this the preferred method of calculation of an integral scale. The results are as follows:

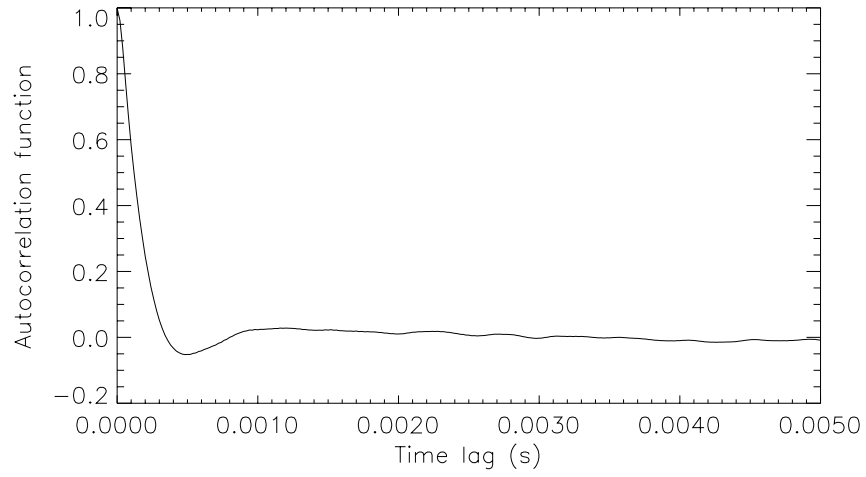
$$f_{u,E_0} = 0.671 \text{ kHz} \quad (11)$$

and

$$f_{v,E_0} = 1.387 \text{ kHz} \quad (12)$$



X-wire: rxw324a02 -- inlet to N1
u-autocorrelation function



X-wire: rxw324a02 -- inlet to N1
v-autocorrelation function

Figure 5: Longitudinal (top) and transverse (bottom) autocorrelation at the inlet of nozzle 1.

in good agreement with the values listed above. The 10% to 20% discrepancy is accounted for by incomplete convergence in the tail of the autocorrelation function and in the low-frequency portion of the spectrum.

2.2 Dominant Frequencies

An alternative characteristic time scale based on the Fourier spectrum is the dominant (most energetic) spectral range. Formulae are reproduced in Appendix 2. It is generally known that the most energetic frequency is identified as the frequency corresponding to the maximum of the $fE_F(f)$ curve. Computations of this statistic are very fast, and accuracy is good as long as the power spectrum shows little scatter. If necessary, smoothing of the power spectrum can be introduced to mitigate the effect of spurious spikes.

Although the definitions of the integral scale (and its corresponding frequency) and of the dominant frequency are not identical, they are related in the sense that the turbulent eddies most closely associated with the integral time scale are the ‘large’ eddies – the ‘*energy-containing*’ eddies. Thus, the integral scale and the dominant scale characterize the same spectral range, and the numerical values should be of the same order of magnitude. Since model constants are adjusted based on the values of integral scales, a quantitative conversion factor from dominant to integral scales is required if the dominant scale is to be used. In appendix 3, a simple analytical model of the power spectrum provides a possible conversion factor. This issue will be addressed further in the conclusions.

The Fourier power spectra for u and v are shown on Fig. 1. The spectra are generally featureless, but the two components are appreciably different. In contrast to the integral scales, a relevant time scale can be defined as a local (pointwise) property of the spectrum, i.e. the scale corresponding to the most energetic eddies. The dominant frequency defined in this manner is easily identified at the peak of $f.E(f)$, as shown on Fig. 6

The experimental scatter in the spectra will lead to some minor differences in the determination of the dominant frequency. From Fig. 6, we get the values

$$f_{Eu} = 0.666 \text{ kHz} \quad (13)$$

and

$$f_{Ev} = 1.188 \text{ kHz}. \quad (14)$$

The values are in close agreement with the integral scales provided above.

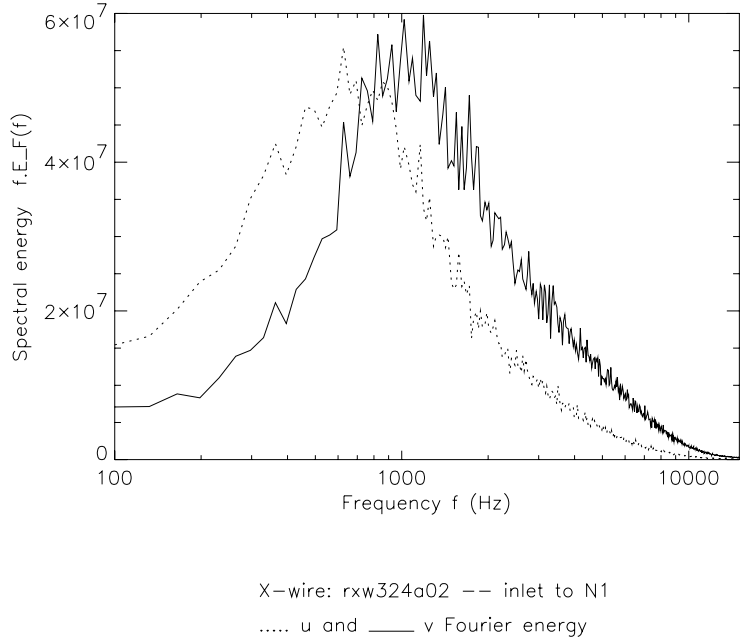


Figure 6: *Longitudinal (dotted line) and transverse (solid line) energy content at inlet of nozzle 1.*

2.3 Wavelet-based dominant scales

Wavelets have emerged in recent years as a useful alternative to Fourier analysis for the case of unsteady data. Some fundamental relations about wavelet analysis are listed in Appendix 4. We apply the wavelet processing to the stationary data to demonstrate the equivalence with Fourier methods in this case. Given this reliability check, the justification for using wavelet methods will be found in the analysis of unsteady data in the next Section.

We used two different wavelets in this analysis (see Appendix 4 for details). The Morlet wavelet is a complex-valued wavelet, most appropriate when local periodicity is expected. The Mexican Hat wavelet is real, and is better suited to identify isolated features in the signal. Temporal localization is best viewed from the time series; spectral features are clearly visible on the Fourier transform. Between these extremes, a combination of temporal and spectral information is captured by wavelets, and different wavelets correspond to a different emphasis on temporal vs. spectral resolution. In this framework, the Morlet wavelet achieves better spectral resolution with poor localization, whereas the Mexican Hat wavelet favors temporal resolution at the cost of some spectral resolution. This point is illustrated by the respective power spectra, in which the smoothness of the Morlet spectrum is intermediate between the Fourier and Mexican Hat spectra (see Figs. 7 and 8). The comparison with Fig. 6 shows excellent agreement between the three methods.

The most energetic frequencies are identified from these figures as

$$f_{u-Mor} = 0.720 \text{ kHz}, \quad (15)$$

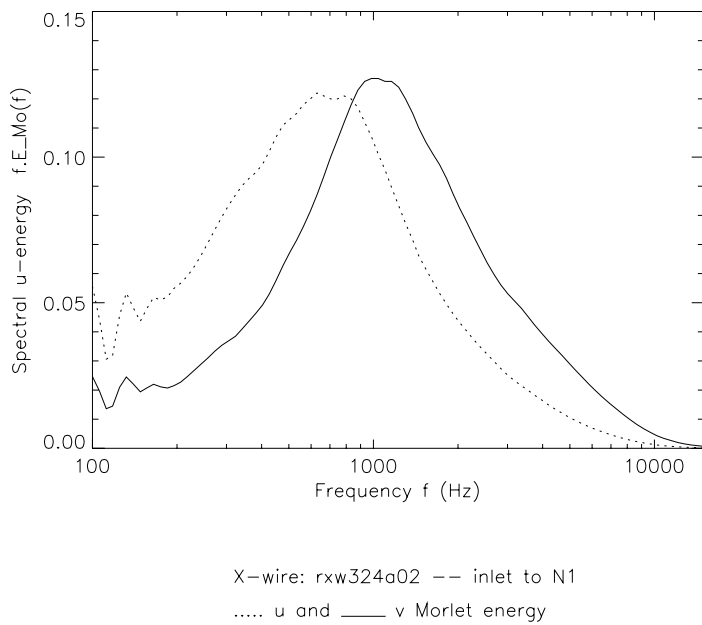


Figure 7: Streamwise (dotted line) and transverse (solid line) Morlet energy content at inlet of nozzle 1.

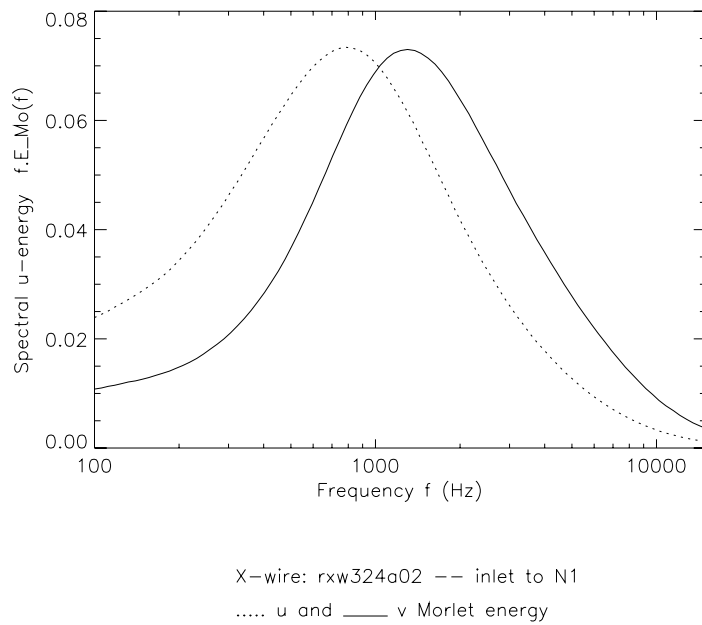


Figure 8: Streamwise (dotted line) and transverse (solid line) Mexhat energy content at inlet of nozzle 1.

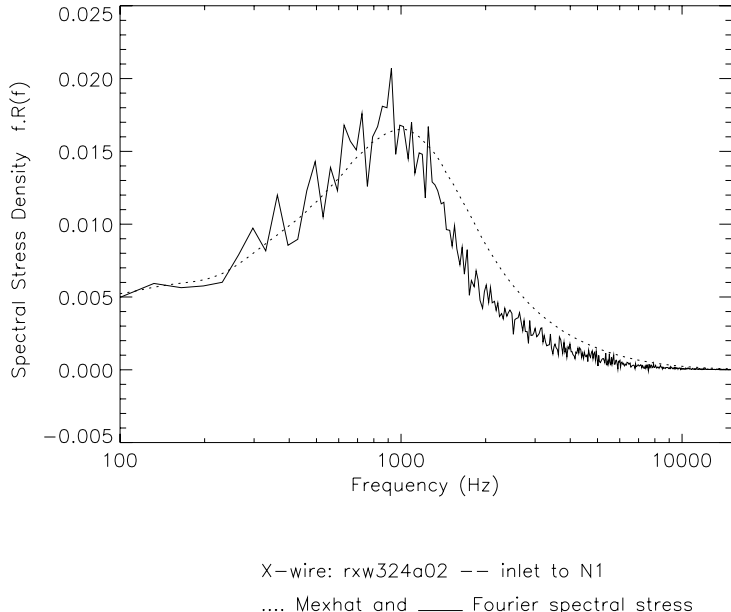


Figure 9: Fourier- (solid line) and Mexhat (dashed line) spectral stress distribution.

$$f_{v-Mor} = 1.079 \text{ kHz}, \quad (16)$$

$$f_{u-Mex} = 0.796 \text{ kHz} \quad (17)$$

and

$$f_{v-Mex} = 1.321 \text{ kHz}. \quad (18)$$

We conclude that the time scales calculated by conventional methods and wavelet results are in agreement.

2.4 Spectral distribution of the turbulent stress

X-probe data enables one to calculate scales relevant to the turbulent transport. Multiplication of the co-spectrum by the frequency yields the spectral stress distribution, shown on Fig. 9

A similar decomposition of the Reynolds stress was presented in AIAA-94-2323, and further analyzed in NASA-TP-3555. The Mexhat stress distribution is also shown on Fig. 9. We note again the general agreement between the two methods. The dominant frequencies are identified, respectively as

$$f_{coFou} = 0.924 \text{ kHz} \quad (19)$$

and

$$f_{coMex} = 0.975 \text{ kHz}. \quad (20)$$

2.5 Comparison and interpretation

To summarize, the numerical values of characteristic or dominant frequencies calculated in the previous subsections are reproduced in tabular form.

Table 1: Comparative table of dominant frequencies at the N1 inlet.

$f_{u,int}$	0.606 kHz
$f_{v,int}$	1.106 kHz
f_{u,E_0}	0.671 kHz
f_{v,E_0}	1.387 kHz
f_{Eu}	0.660 kHz
f_{Ev}	1.188 kHz
f_{coFou}	0.924 kHz
f_{u-Mor}	0.720 kHz
f_{v-Mor}	1.079 kHz
f_{u-Mex}	0.796 kHz
f_{v-Mex}	1.321 kHz
f_{coMex}	0.975 kHz

The numerical values of possible relevant frequencies fall into three main categories.

1. Longitudinal (streamwise) scales fall in the range of 0.606kHz to 0.796kHz . The lower value suffers the most from known problems associated with the accuracy in the tail of the autocorrelation function, and may be ignored. The frequency 0.671kHz should be preferred in relation to the integral scale. Energy-dominant scales are then 0.660kHz for the Fourier spectrum (affected by the spurious peaks resulting from incomplete convergence), 0.720kHz from the Morlet spectrum and 0.796kHz from the Mexican Hat spectrum.
2. Transverse components yield larger values. We already noted that, in isotropic turbulence, a factor of 2 would be expected, so the inlet turbulence results are consistent with nearly-isotropic turbulence. The most reliable value from autocorrelation is 1.387kHz , while the Mexican Hat dominant frequency is 1.321kHz , a 5% discrepancy.
3. Finally, values of the frequency contributing the largest part of the Reynolds stress is intermediate between the above.

We conclude that

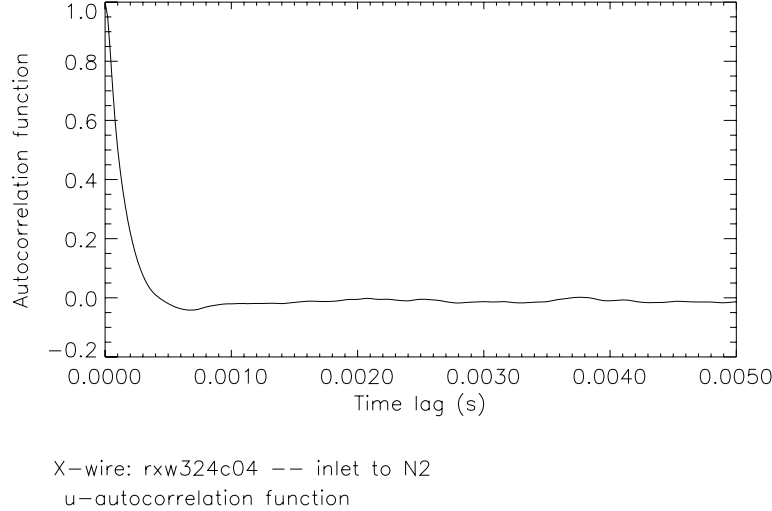


Figure 10: *Longitudinal autocorrelation at the inlet of the second stage (N2).*

1. while the Reynolds stress scales are consistent with the u- and v-scales, their use is subject to data availability and presents no obvious advantage over the 1-component alternatives.
2. differences between the u- and v-components are expected from the theory of isotropic turbulence.
3. the integral scale method and wavelet method yield results within 7% of each other.

Having shown the equivalence of the methods when applied to stationary turbulence, we now turn to the unsteady case.

3 Unsteady Flow at the R1 Exit Section

3.1 Further Validation for Mean Time Scales

The streamwise (longitudinal) autocorrelation function is shown on Fig. 10. We note the negative values of the autocorrelation within time lags of approximately .3 ms. This overshoot leads to the partial cancelation of the integral (Eq. 3). This problem is combined with statistical fluctuations in the ‘tail’ (large time lags) of the autocorrelation, and leads to inaccurate values of the integral scale. This problem is alleviated by the extrapolation of E_1 to low frequencies; only these values will be tabulated below.

The Fourier energy distributions for streamwise and transverse fluctuations are shown on Fig. 11. The N1 results (Fig. 6) are shown to scale. The relative magnitudes of the incoming and wake-induced turbulence can be observed, as is the shift toward higher frequencies. However, the separation in scale is not sufficient to identify the scales as distinct on these figures. We see a general shift toward higher frequencies, particularly in the case of the transverse component. This result is true also for the Morlet- and Mexhat energy distributions, not shown here.

A different picture emerges from the spectral distributions of Reynolds stress. Fig. 12 shows the Fourier- and Mexhat versions. Beside the good agreement between the two methods, the changes from the N1 inlet are noteworthy. The stress distributions are in fact double-peaked, with a low-frequency peak identified at 500 Hz (the wake-passing frequency, in spite of the subtraction of the ensemble mean), separated from a weaker peak in the 5 kHz range by a spectral range of weakly negative correlations. Further study will determine how spectral regions can be associated more clearly with the wake passings.

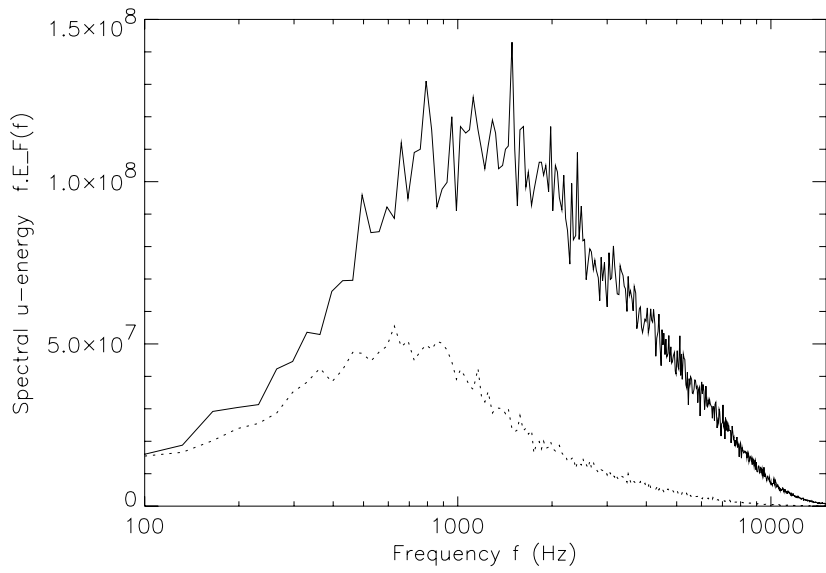
As for the N1 data, the characteristic frequencies are tabulated below for easier comparison.

Table 2: Comparative table of dominant frequencies at the N2 inlet.

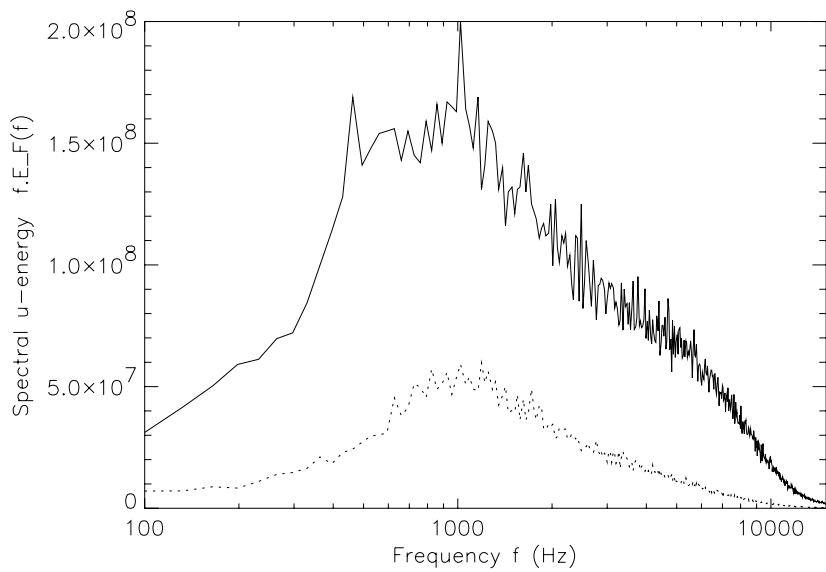
f_{u,E_0}	1.254 kHz
f_{v,E_0}	0.991 kHz
f_{Eu}	1.122 kHz
f_{Ev}	1.023 kHz
f_{coFou}	.528 kHz
f_{u-Mor}	1.079 kHz
f_{v-Mor}	.975 kHz
f_{u-Mex}	1.390 kHz
f_{v-Mex}	1.079 kHz
f_{coMex}	.559 kHz

3.2 Comparison and interpretation

The first observation on Table 2 is that the 2:1 ratio of longitudinal to transverse scales predicted by the theory of isotropic turbulence no longer holds true. Second, the methods based on single components of velocity agree with each other. Finally, the dominant scale in the spectral distribution of Reynolds stresses is surprisingly low, and very close to the wake passing frequency.



X-wire: rxw324c04 -- inlet to N2
u-Fourier power spectrum



X-wire: rxw324c04 -- inlet to N2
v-Fourier power spectrum

Figure 11: Streamwise (top) and transverse (bottom) energy content at inlet of nozzle 2. The nozzle 1 results are reproduced in dotted line.

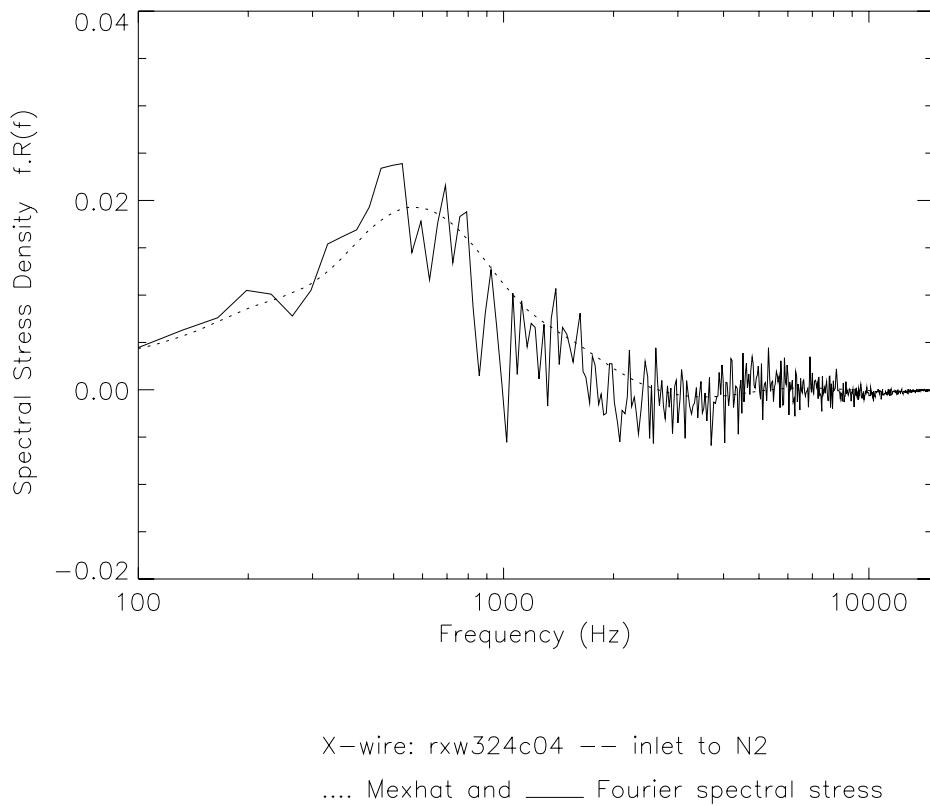


Figure 12: *Spectral stress distribution: Fourier (solid line) and Mexhat wavelet (dotted line).*

Even if we overlooked this last point, the characterization of the data is as yet unsatisfactory. The spectral stress distribution can be taken as an example (Fig. 12). Three scales are identified — two associated with positive correlations of u and v , separated by a negatively correlated patch of scales. It is clear that several flow phenomena are at play, but the time averages do not allow us to separate them. Given the flow conditions, we surmised that the different spectral ranges are associated with the unsteady wake-passing. A phase conditioning similar to that reported in Schobeiri et al. [14] is indicated, and is the object of the following section.

3.3 Conditional Scales from Wavelet Processing

One of the dominant features in the preceding sections is the overall agreement between the various (Fourier vs wavelet) methods. However, it is clear by inspection of the raw data, and also from the wavelet maps shown in Section 2, that the characteristics of the fluctuations are modulated by the wake passings. To associate a unique frequency with these fluctuations is bound to mask some of the flow physics.

The key to the determination of local time scales is found in the wavelet methods. A variant of the conditional sampling method introduced in Higuchi et al. [8] and used in Schobeiri et al. [14], was developed for this study. It consists of calculating the norm-Morlet transform² of the ensemble mean, finding its dominant frequency f^+ , and calculating its phase $\phi(f^+, t)$ at that frequency and as a function of time; see Walker et al. [15] for details and examples. Then, the time-integral of energy in the Parseval relation (Eq. 24) is restricted to those contributions that coincide with a narrow range of phases: essentially, we construct phase-locked energy distributions, i.e. the signal's energy content as a function of frequency and phase relative to the ensemble mean.

The algorithm is as follows. The ensemble average velocity was constructed, and its dominant frequency (500 Hz, corresponding to the blade passing frequency) determined. Then, the phase-Morlet transform gave the phase of the ensemble average as a function of time. For a sinusoidal signal, the phase history would consist of a straight line increasing by 2π per period, with periodic resets ($\text{mod}(2\pi)$). This yields a uniform probability distribution of the phase angle of the interval $(0, 2\pi)$. The phase distribution for the ensemble velocity (streamwise, say) at the R1 exit is very nearly uniform. In the expressions of the wavelet energy and stress distributions (Eqs. 45

²From Eqs. 42 and 43, it is evident that the Morlet wavelet transform is a complex function of the real variables κ and t . The norm of this function contains the energy information (see Parseval's theorem, above), while *local* phase information is defined by the polar angle between the real and imaginary parts:

$$u_g(f, t) = u_{norm}(f, t) e^{i\phi(f, t)} \quad (21)$$

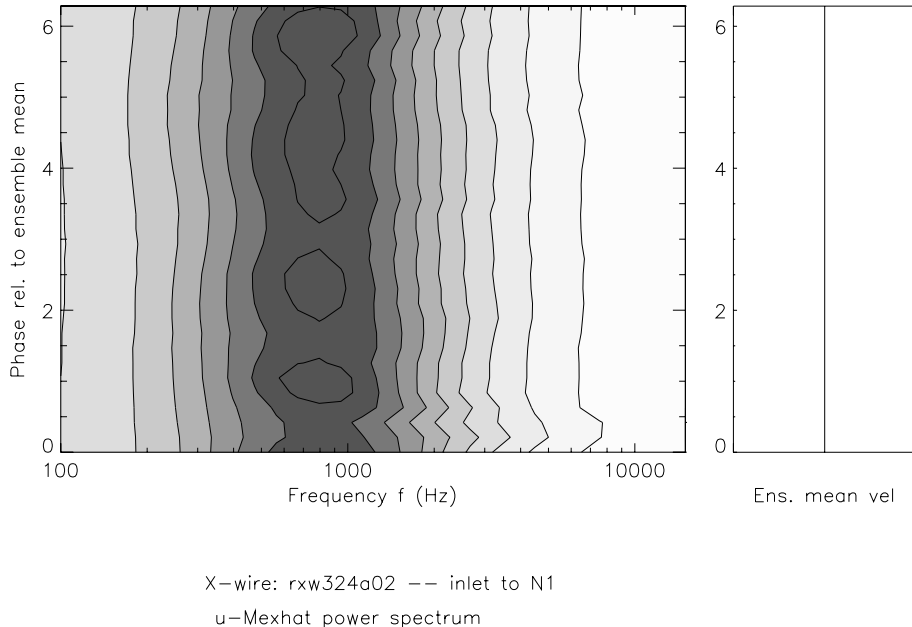


Figure 13: *Streamwise frequency/phase Mexhat energy distributions at the N1 inlet. Morlet statistics are very similar.*

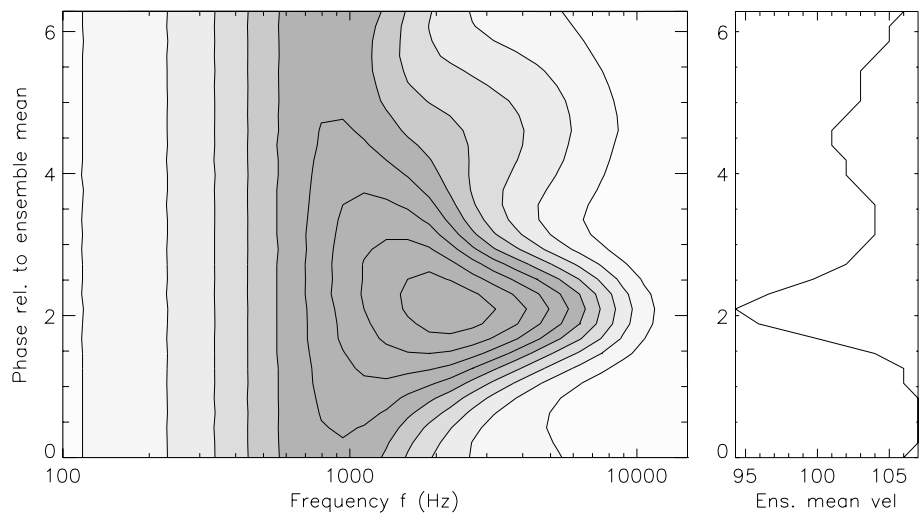
and 48), the time integral can be restricted to a given phase, and the distributions plotted as a function of this phase. The result is examined in this section.

At the N1 inlet section, where there are no wakes and the ensemble average velocity is extremely small, the dominant scales can be expected to be independent of the phase. Indeed, Fig. 13 shows the frequency/phase energy content of the signal, with the dominant time scale at approximately 700 Hz corresponding to the average. Similar results are obtained for the transverse component, using either Morlet or Mexhat wavelets; and also for the the Reynolds stress distribution.

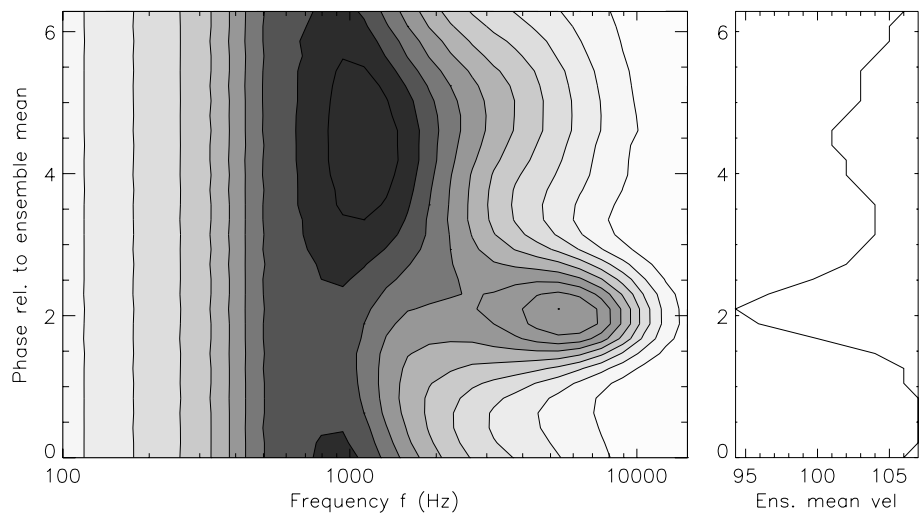
These results are in sharp contrast to the R1 exit data. Here, the wakes of N1 (chopped by the R1) and R1 pass at the measuring station periodically, and are associated with very different dominant scales.

Fig 14 shows the frequency/phase energy content of the fluctuations. For the streamwise component, a roughly uniform phase distribution corresponding to the average peak is observed around 1 kHz. More energetic fluctuations at a higher frequency (3 to 5 kHz) are observed around $\phi = 2$. By comparison with the ensemble mean signals (Fig. 7), we associate this smaller-scale turbulence with the rotor wakes. The transverse component shows stronger phase dependence of the energy content. The wake turbulence is now seen at higher frequencies (5 kHz), while the dominant mean peak is seen to result from contributions from phase angles larger than π .

A slightly different picture emerges from the Mexhat analysis. Fig. 15 shows a very strong phase localization of the streamwise energy distribution around $\phi = 2$, with weaker fluctuations for the remainder of the period. In contrast, the transverse component shows a nearly uniform (mean) distribution for all phases, and an isolated

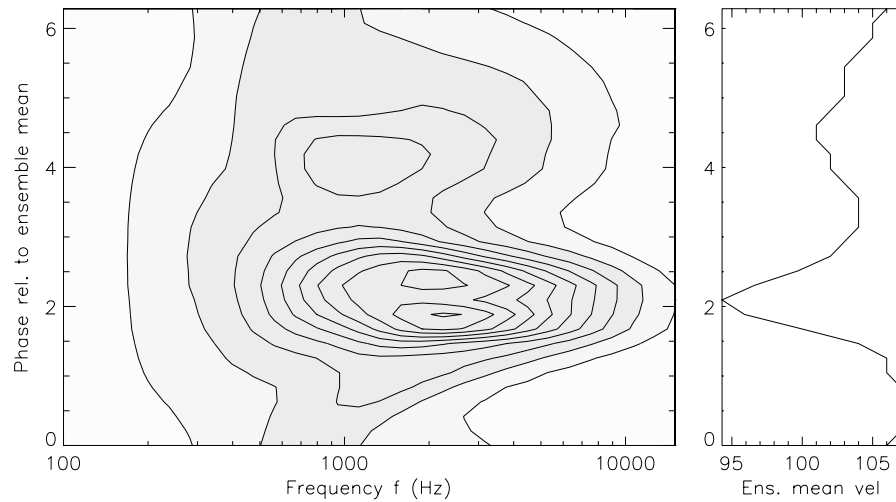


X-wire: rxw324c04 -- inlet to N2
u—Morlet power spectrum



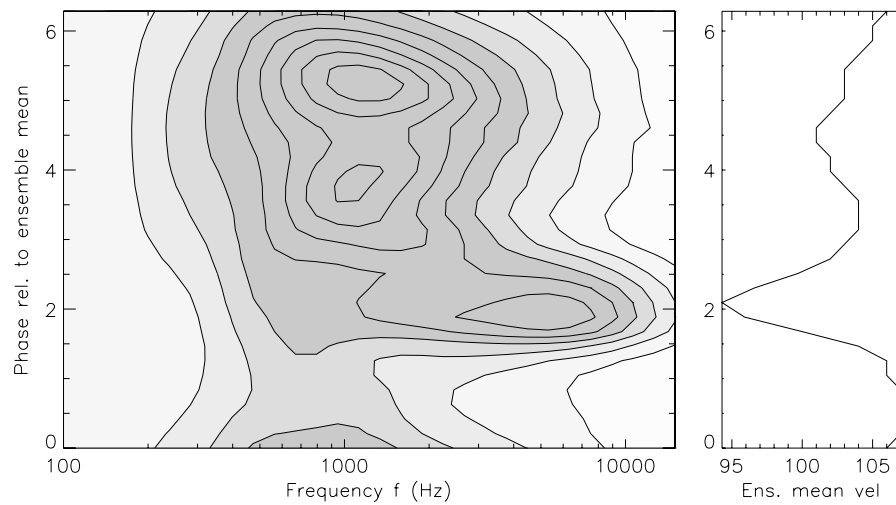
X-wire: rxw324c04 -- inlet to N2
v—Morlet power spectrum

Figure 14: Streamwise (top) and transverse (bottom) frequency/phase Morlet energy distributions at the R1 exit.



X-wire: rxw324c04 --- inlet to N2

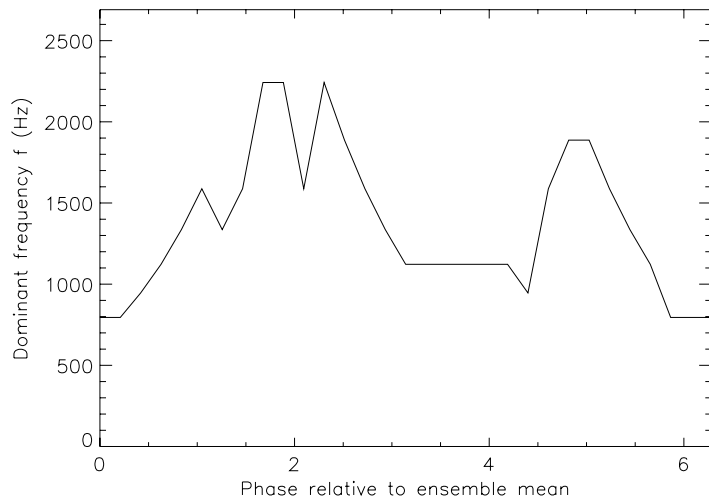
u—Mexhat power spectrum



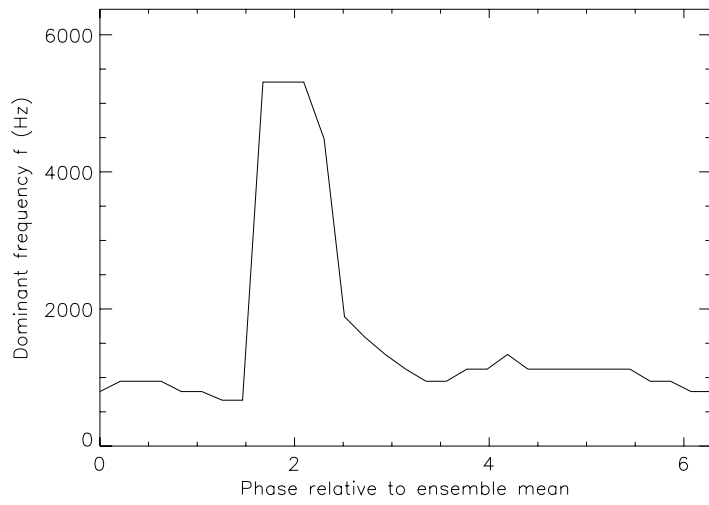
X-wire: rxw324c04 --- inlet to N2

v—Mexhat power spectrum

Figure 15: Streamwise (top) and transverse (bottom) frequency/phase Mexhat energy distributions at the R1 exit.



X—wire: rxw324c04 — inlet to N2
u—Mexhat power spectrum



X—wire: rxw324c04 — inlet to N2
v—Mexhat power spectrum

Figure 16: Streamwise (top) and transverse (bottom) most-energetic-frequency as a function of phase at the R1 exit.

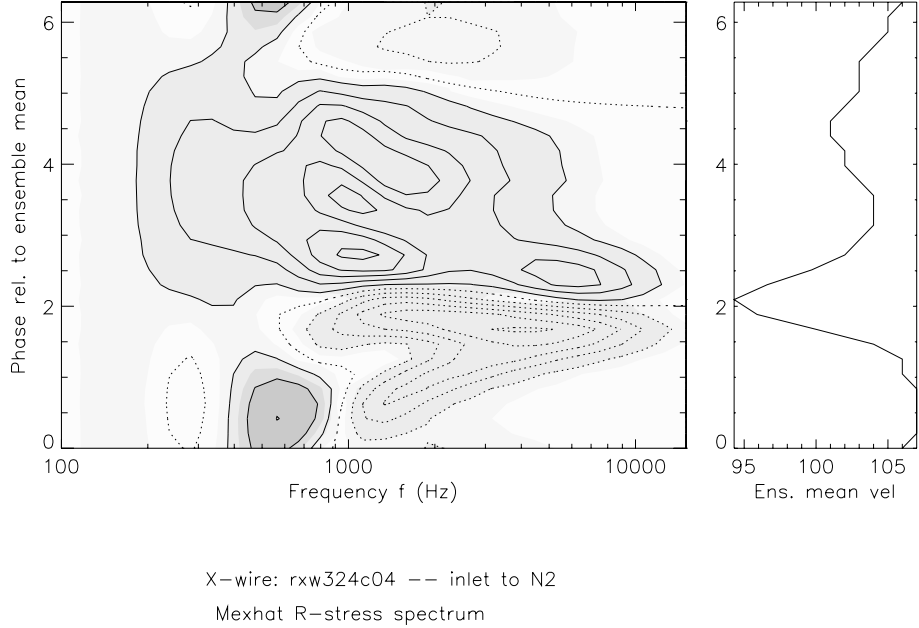


Figure 17: Frequency/phase Mexhat stress distributions at the R1 exit.

island at much higher frequency at the phase of the wake passing.

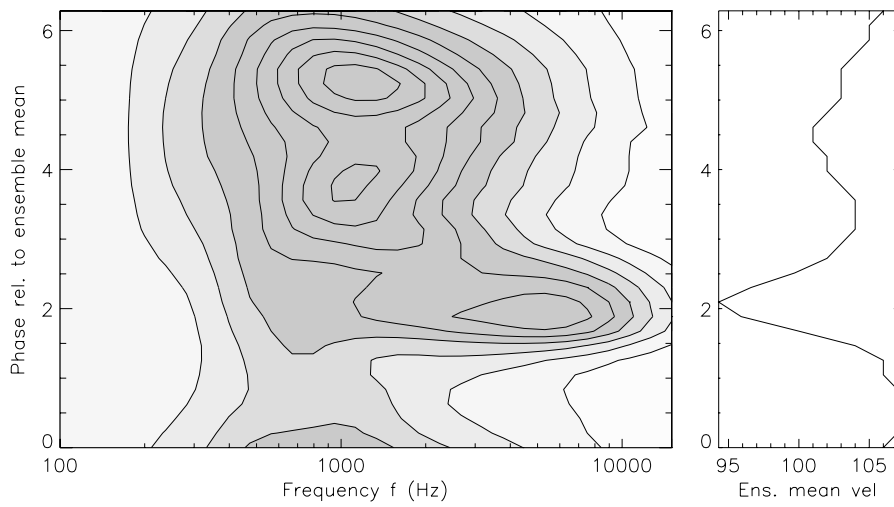
The most energetic frequency (the ‘ridge’ on Fig. 15) is plotted on Fig. 16. We see a doubling of the dominant frequency at $\phi = 2$, for both components of velocity. The peak is more sharply defined for the transverse component. The streamwise component shows another increase (missing from the v-data) out-of phase with the wake-passing by $\pi/2$.

Finally, the stress distribution is shown on Fig. 17. We see the sign reversal of the stress almost exactly at $\phi = 2$. We interpret this reversal as matching the change in sign of the ensemble mean velocity gradients across the wake. We also see that the dominant scales on either side of the wake are not equal. The larger scales at $\phi > 2$ could be associated with the N1 wakes, and the yet larger ones at $\phi < 1$ remain to be interpreted.

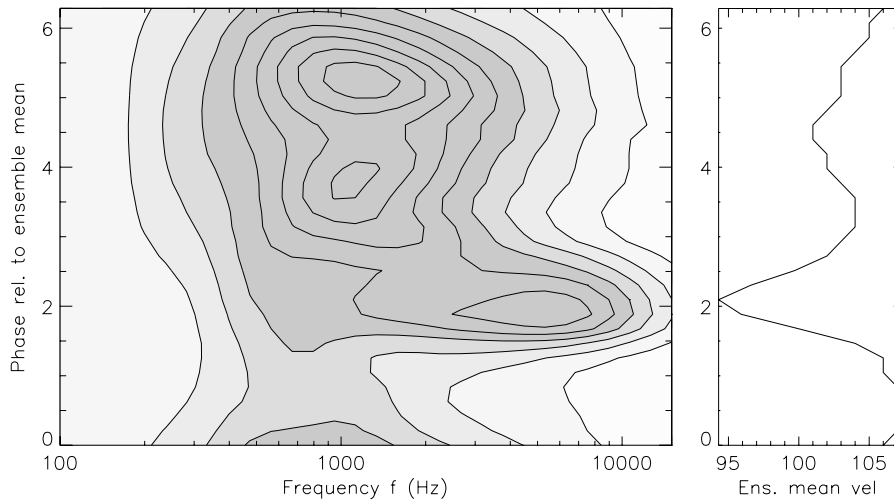
The next series of figures (18 and 19) show the phase-dependent energy content, and the dominant frequencies, for the raw data, including the ensemble velocities. Although the dominant frequencies are slightly lower than with the ensemble velocity subtracted, the wake passing frequency (about 500 Hz) is not dominant.

3.4 Discussion

The calculation of the frequency/phase energy and stress plots relies on the conditional sampling of the energy maps, i.e. the time-frequency distribution of energy. It may be possible to achieve this result with windowed Fourier transforms, but wavelet transforms are the natural technique to reach this goal. Having ascertained that Fourier and wavelet methods given essentially the same results with the more sta-



X—wire: rxw324c04 — inlet to N2
v—Mexhat power spectrum



X—wire: rxw324c04 — inlet to N2
v—Mexhat power spectrum

Figure 18: *Streamwise (top) and transverse (bottom) frequency/phase Mexhat energy distributions at the R1 exit.*

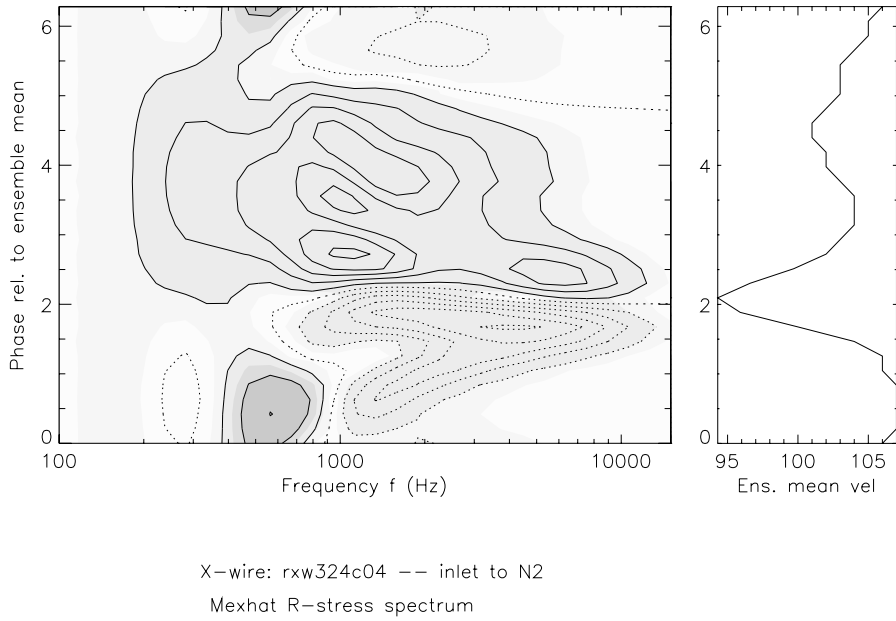


Figure 19: *Frequency/phase Mexhat stress distributions at the R1 exit.*

tional signals at the N1 inlet, we are justified in using the better-suited wavelet tools at the N2 inlet.

Morlet and Mexhat results, both for energy and Reynolds stress, agree that the dominant scales vary with the phase of the wake-dominated ensemble mean velocity, and that the scales are appreciably shorter at a phase $\phi \sim 2$ corresponding to the smallest values of the streamwise ensemble velocity, i.e. the wake passings. Therefore, we conclude that the frequency/phase plots discriminate quantitatively between freestream and wake turbulence, their energy content and dominant frequencies — parameters at the core of $\kappa-\varepsilon$ unsteady models.

However, there are differences in the particulars of the distribution of energy in the frequency/phase plane depending on the wavelet. This is a reminder that spectral methods project the signal on a template: infinite complex sine wave in Fourier transforms, a wave packet in Morlet wavelet transforms, a single bump in the case of Mexhat wavelet transforms. The key underlying issue is the trade-off between frequency and time resolution — heuristically associated with Heisenberg’s uncertainty principle. The progression from Fourier to Morlet (with decreasing values of z_0) to Mexhat corresponds to increasingly accurate temporal localization of ‘events’, at the expense of a deteriorating spectral accuracy. The user should choose the best tool accordingly. In our case, we see no reason to assume even local periodicity of the fluctuations around the ensemble mean, and the Morlet template appears somewhat contrived (an unrealistic model for local fluctuations); we view the Mexhat results as most informative.

4 Conclusions

In this report, we have accomplished three things:

1. We have developed flexible alternatives to the integral time scales as a way to characterize unsteady data. We have shown that the various definitions yield comparable results on modeled spectra. We also show agreement between integral scales and dominant scales for all data sets available for this preliminary study.
2. Having established that wavelet tools yield results equivalent to Fourier methods, we used the time-frequency resolution of wavelets to map phase-dependent properties. We were able to quantify spectral energy content and dominant frequencies as a function of phase. Thus, the effect of wake passing at the N2 inlet could be characterized.

The experimental data made available to us by GE are very rich in flow physics pertaining to wake-induced transition on compressor blades. An obvious application of this information in the construction and testing of improved models for unsteady transition, and the comparison of model and experimental results.

Given the reliance of modelers on the integral scale, it would be desirable to provide a conversion factor between the integral and the dominant scales. As expected, the ratio of these scales turns out to be of the order of 1 in all cases where both can be calculated. A more detailed comparison leads to the following table:

Table 3: Conversion factor from integral to dominant frequencies. These values should be compared to the $\sim .75$ number obtained in Appendix 3.

N1	$f_{u-Mor}/f_{u,E_0}$	0.720 / 0.671 = 1.07
N1	$f_{v-Mor}/f_{u,E_0}$	1.079 / 1.387 = 0.78
R1	$f_{u-Mor}/f_{u,E_0}$	1.079 / 1.254 = 0.86
R1	$f_{v-Mor}/f_{u,E_0}$	0.975 / 0.991 = 0.98
N1	$f_{u-Mex}/f_{u,E_0}$	0.796 / 0.671 = 1.18
N1	$f_{v-Mex}/f_{u,E_0}$	1.321 / 1.387 = 0.95
R1	$f_{u-Mex}/f_{u,E_0}$	1.390 / 1.254 = 1.11
R1	$f_{v-Mex}/f_{u,E_0}$	1.079 / 0.991 = 1.09

We note that the Mexhat statistics tend to be slightly larger than comparable Morlet statistics, and that all values are larger than the .75 expected from the Pao model in Appendix 3. It is apparent that the particulars of the spectral distribution of energy, and the particulars of the analyzing wavelet, introduce some variability

in the quantitative result. This variability is inherent in the statistical reduction of complex information to simple numbers. The real question lies in the impact this variability may have on modeling. Experience will tell what adjustments to model constants, if any, are required to ensure agreement between wavelet-dominant scales and modeling outcomes. The fact remains that, in the unsteady environments encountered in turbomachinery and other complex flows, conventional definitions cease to be meaningful; this report is a first step in devising alternatives.

References

- [1] R.A. Antonia (1981), ‘Conditional sampling in turbulence measurement’, *Ann. Rev. Fluid Mech.* 13, 131-156.
- [2] I. Daubechies (1992), ‘Ten Lectures on Wavelets’, S.I.A.M.
- [3] M. Farge (1992), ‘Wavelet Transforms and their Applications to Turbulence’, *Annual Reviews of Fluid Mechanics* 24, 395-457.
- [4] D.E. Halstead, D.C. Wisler, T.H. Okiishi, G.J. Walker, H.P. Hodson and H.-W. Shin (1995), ‘Boundary layer development in axial compressors and turbine’, Parts 1-4, ASME Papers 95-GT-461/462/463/464). Also published in *Journal of Turbomachinery, Transactions of the ASME*: Part 1: vol. 119, no. 1, 114-127, Part 2: January 1997; vol. 119, no. 3, 426-444, July 1997; Part 3: Vol 119, no. 2, 225-237, Apr 1997; Part 4: vol. 119, no. 1, 128-139, January 1997.
- [5] D.E. Halstead, ‘Boundary layer development in multi-stage low pressure turbines’, PhD Thesis, Iowa State University, 1996.
- [6] T.B. Hedley and J.F. Keffer (1974), ‘Turbulent/non-turbulent decisions in an intermittent flow’, *J. Fluid Mech.* 64, 625-644.
- [7] J.O. Hinze (1975), *Turbulence*, McGraw Hill.
- [8] H. Higuchi, J. Lewalle and P. Crane (1994), ‘On the Structure of a Two-Dimensional Wake behind a Pair of Flat Plates’, *Phys. Fluids A* 6, 297-305.
- [9] J. Lewalle (1994), ‘Wavelet transforms of some equations of fluid mechanics’, *Acta Mech.* 104, 1-25.
- [10] J. Lewalle (1994), ‘Wavelet Analysis of Experimental Data: Some Methods and the Underlying Physics’, AIAA Paper 94-2281.
- [11] J. Lewalle and D.E. Ashpis (1997), ‘Demonstration of wavelet techniques in the spectral analysis of bypass transition data’, NASA TP-3555.
- [12] J. Lewalle (2000), ‘Detection, Tracking and Analysis of Turbulent Spots and Other Coherent Structures in Unsteady Transition’, NASA CR-2000-210694.
- [13] Y. Meyer (1993), ‘Wavelets: algorithms and applications’, S.I.A.M.

- [14] M.T. Schobeiri, K. Read and J. Lewalle (1995), 'Effect of Unsteady Wake Passing Frequency on Boundary Layer Transition, Experimental Investigation and Wavelet Analysis', ASME Paper 95-GT-437.
- [15] S.H. Walker, S.V. Gordeyev and F.O. Thomas (1995), 'A wavelet transform analysis applied to unsteady jet screech resonance', ASME Fluids Engineering Conf.
- [16] D.C. Wilcox, (1993) 'Turbulence Modeling for CFD', DCW Industries, 1993.

Appendix 1 — Integral Scales

Let us focus first on one velocity signal, say $u(t)$. Its standard deviation is measured by u' (see Eq. 1). One of the relevant time scales is characteristic of the persistence of correlations between lagged signals, measured by the autocorrelation function. The longitudinal autocorrelation function for a stationary signal $u(t)$ is defined by Eq. 2. The autocorrelation functions measure the gradual loss of correlation as the time lag between measurements of the given component u increases. Analytical and experimental properties of these functions can be found in standard references [7]. For diagnostic purposes, it is convenient to summarize the information about the drop-off by a single number: the longitudinal integral time scale is defined by Eq. 3. Practically, the computation of the autocorrelation function is very time consuming. Furthermore the slow convergence of the function for large times makes its numerical integration rather inaccurate. For these reasons, an alternative definition is generally preferred. Start from the Fourier transform $\hat{u}(f)$ of the signal $u(t)$:

$$\hat{u}(f) = \int_{-\infty}^{\infty} u(t) e^{-2i\pi f t} dt \quad (22)$$

Then, the Parseval theorem,

$$\int_{-\infty}^{\infty} |u(t)|^2 dt = \int_{-\infty}^{\infty} df |\hat{u}(f)|^2, \quad (23)$$

leads to the definition of the power spectrum. Following Hinze (p.57), we define $E_F(f)$ by the relation

$$u'^2 = \int_0^{\infty} E_F(f) df, \quad (24)$$

Then it is easy to show (e.g. Hinze [7], p65) that the integral scale defined above can be calculated from Eq. 10. The convergence problem for the autocorrelation function now takes the form of inaccuracies in the calculation of the low-frequency part of the spectrum. However, as the energy density is constant in this region of the spectrum, extrapolation of any well-converged part region of the spectrum, extrapolation of any well-converged part of the spectrum to lower frequencies gives reliable estimates of $E_F(0)$. Thanks to the use of FFT's, the integral scales can be calculated very efficiently.

In the case of digital time series, the formulae are adapted as follows. We denote by u_i , $i = 0, \dots, (N - 1)$ the N values of velocity collected at time intervals Δ so that $t_i = (i - 1)\Delta$. It is assumed that u_i has zero mean. Then

$$u'^2 = \frac{1}{N} \sum_0^{N-1} u_i^2 \quad (25)$$

The autocorrelation function is defined as

$$f_i^u = \frac{1}{Mu'^2} \sum_{j=0}^{M-1} u_j u_{j+i} \quad (26)$$

where M and the range of i 's are restricted to match the number of data points. For example, if $M = N/2$, f_i will be defined over the range $i = 1, \dots, (N/2 - 1)$. Then, the integral scale is given by

$$T_{u,int} = \frac{2\Delta}{N} \sum_0^{N/2-1} f_i^u \quad (27)$$

The discrete Fourier transform can be calculated over the frequency scale $f_i = (i - 1)/\Delta$ by the formula

$$\hat{u}_i = \sum_{j=0}^{N-1} u_j e^{2i\pi f_i t_j} \Delta \quad (28)$$

and the discrete power spectrum is defined as

$$E_i^F = \hat{u}_i^2. \quad (29)$$

Under these definitions, we have

$$u'^2 = \sum_0^N E_i^F / Delta \quad (30)$$

and the integral scale can be calculated as

$$T_{u,int} = \lim_{i \rightarrow 0} \frac{E_i^F}{4u'^2} \quad (31)$$

(see Hinze [7], p.65).

Appendix 2 — Dominant Scales

An alternative characteristic time scale based on the Fourier spectrum is the dominant (most energetic) spectral range. The spectral energy content in a logarithmic frequency band around f is estimated by the integral

$$\Delta E_F(f) = \int \int_{\Delta f} E_F(f) df = \int_{\Delta \log f} f E_F(f) d(\log f), \quad (32)$$

Accordingly, dominant scales are identified as the maxima of $fE_F(f)$. Let us denote the dominant frequency as

When two signals are available the cross spectrum can be computed. The spectral distribution of u-v-correlations is obtained from the corresponding Parseval formula (of which Eq.(24) is a particular case):

$$\begin{aligned} - \int_{-\infty}^{\infty} u(t)v^*(t)dt &= - \int_{-\infty}^{\infty} \hat{u}(f)\hat{v}^*(f) f = - \int_{-\infty}^{\infty} f \hat{u}(f)\hat{v}^*(f) d\log(f) \\ &= \int_{-\infty}^{\infty} f R_F(f) d\log(f). \end{aligned} \quad (33)$$

The asterisk denotes complex conjugation. The expression $-f\hat{u}(f)\hat{v}^*(f) = f R_F(f)$ is therefore a measure of the spectral distribution of Reynolds stress. Any peaks of this function identify dominant scales, as used in the text.

Appendix 3 — Comparison of Integral and Dominant Scales

This section addresses the differences between the integral and dominant scales defined above. There is no reason why the two methods would give the same result, but it is important that results can be compared. We will establish a basis for comparison by calculating the corresponding time/frequency scales from a simple expression of the power spectral density. We note that the formulae use wavenumber rather than frequency (to give the correct slope of the inertial spectrum), and that the spatial Fourier transform underlying these manipulations rely on the wavefunctions $\exp(i\kappa x)$ rather than $\exp(2i\pi kx)$. This difference with the formulae used for the frequency spectrum are consistent with Hinze's notations, and results minor difference of appearance between the spatial and temporal relations. For example, the length scale L_{max} corresponding to a dominant wavenumber κ_{max} is given by

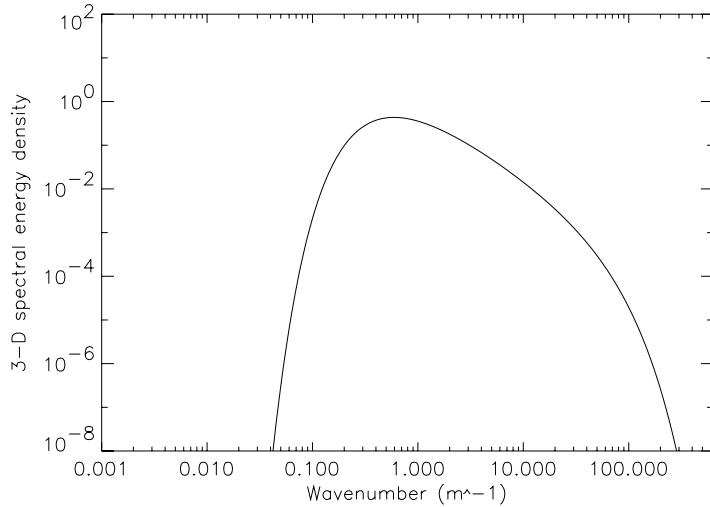
$$L_{max}\kappa_{max} = 1 \quad (34)$$

to be contrasted with Eq.(8).

A variant on the model of Pao (Hinze [7], p 240) will be used here, modifying a 3-D Kolmogorov spectrum to account for large- and small-scale effects. The 3-D energy spectrum we will use is

$$E_3(\kappa) = \alpha \varepsilon^{2/3} \kappa^{-5/3} \exp(-(\kappa\eta)^{4/3}) \exp(-(\kappa L)^{-4/3}) \quad (35)$$

where L is the size of the large eddies, η is the Kolmogorov microscale, and α is the Kolmogorov constant. A representative 3-D spectrum calculated from this formula is shown on Fig. 20.



E3Pao

Figure 20: Model of 3-D power spectral density for $Re = 300$.

The parameters ε , u , L , ν and η are related through the definitions

$$\varepsilon = u'^3/L, \quad (36)$$

and

$$\eta = L\left(\frac{u'L}{\nu}\right)^{-3/4} \quad (37)$$

Accordingly:

$$E_3(\kappa) = \alpha u'^2 (\kappa L)^{-2/3} \kappa^{-1} \exp(-(\kappa\eta)^{4/3}) \exp(-(\kappa L)^{-4/3}). \quad (38)$$

Based on the formulae for isotropic spectra (Hinze [7], p 209) we calculated the equivalent 1-D spectrum E_1 , in which directional aliasing results in constant value of E_1 at low frequencies:

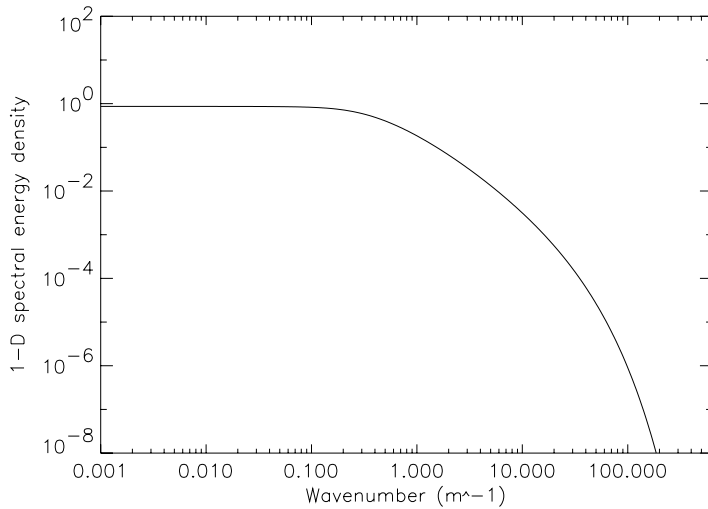
$$\begin{aligned} E_1(\kappa_1) &= \int_0^\infty \frac{E_3(\kappa)}{\kappa} \left(1 - \frac{\kappa_1^2}{\kappa^2}\right) d\kappa \\ &= \alpha u'^2 \int_0^\infty \frac{(\kappa L)^{-2/3} \kappa^{-1} \exp(-(\kappa\eta)^{4/3}) \exp(-(\kappa L)^{-4/3})}{\kappa} \left(1 - \frac{\kappa_1^2}{\kappa^2}\right) d\kappa \end{aligned} \quad (39)$$

The resulting 1-D spectrum is shown on Fig. 21. The normalization condition

$$u'^2 = \int_0^\infty E_1(\kappa) d\kappa \quad (40)$$

yields a value of the Kolmogorov constant α .

Two degrees of freedom are associated with these spectra: we chose to fix L and vary $Re = u'L/\nu$ as the independent parameter.



E1Pao

Figure 21: Model of 1-D power spectral density for $Re = 300$.

The estimates of the integral length scale L' (see Hinze [7], Eq. 3-74):

$$L_{int} = \frac{\pi E_1(0)}{2u'_1^2} \quad (41)$$

and of the most-energetic scale L_{max} defined by the maximum of $\kappa_1 E_1(\kappa_1)$ were obtained numerically. The ratio of these length scales is equal to the inverse ratio of frequencies used on the data, since a common convection velocity is used (Taylor's hypothesis) to convert from length- to time-scale. For a range of turbulence Reynolds numbers, the integral and dominant scales and their ratio are shown on Table 4.

Table 4: Comparison of integral and dominant length scales for a model spectrum.

Re	L_{int}/L	L_{max}/L	L_{int}/L_{max}
30	0.99	1.60	.62
100	1.04	1.50	.69
300	1.06	1.45	.73
1000	1.06	1.42	.75
3000	1.07	1.41	.76
10000	1.07	1.45	.74
30000	1.07	1.45	.74
100000	1.07	1.45	.74

Thus, under Taylor's hypothesis, the characteristic frequencies associated with integral scales would be about 30% as large as frequencies of the most-energetic range,

and the ratio can be expected to be almost independent of the Reynolds number of the turbulence. Therefore, we conclude that for an isotropic turbulence the values of the two large scales are comparable; while referring to different physical content (definitions), they characterize the same dynamical range in a way that is weakly dependent on the Reynolds number of the turbulence³. However, the question of which scale is preferable will arise when we analyze the experimental data below.

Appendix 4 — Wavelet Transforms and Spectra

A wavelet $g(t)$ is a function that meets the admissibility criterion [2]. The wavelet transform u_g of a signal $u(t)$ is

$$u_g(\kappa, t) = \int_{-\infty}^{\infty} \kappa^{1/2} u(\tau) g^*(\kappa(\tau - t)) d\tau. \quad (42)$$

The localization of the wavelet is governed by the variable t , and its duration by κ^{-1} . The significant contributions to the integral is from the regions near the center of the wavelet. The magnitude of the wavelet transform $u_g(\kappa, t)$ reflects how the shape of the wavelet matches the local shape of the signal, other things being equal.

In this study, we used two types of wavelets:

1. The Morlet wavelet is defined by the relation

$$\phi(x, z_0) = (\cos 2\pi x + i \sin 2\pi x) \cdot \exp(-2x^2\pi^2/z_0^2) - \exp(-z_0^2/2 - 2x^2\pi^2/z_0^2), \quad (43)$$

i.e. a complex oscillation of unit frequency with a Gaussian envelope of half-width $1./z_0$. The selection of z_0 reflects a compromise between time- and frequency-localization. A value between 5 and 10 is usually adopted, and we have used $z_0 = 5$ for all calculations reported below. The Morlet wavelet is shown on Fig. 22.

2. The Mexican-hat wavelet (Mexhat below) is distinguished by a single bump, represented analytically by

$$g_2(z) = (z^2 - 1) \exp(-z^2/2), \quad (44)$$

and also shown on Fig. 22. It provides better temporal localization than the Morlet wavelet, at the expense of the frequency resolution.

³In the case of the GE data, the relevant factor in this comparison will be the ‘effective Reynolds number’, with the frequency cut-off of the data playing the role of the Kolmogorov microscale. For example, with a ratio of the order of 20 between the energetic eddies and the cut-off, the effective Reynolds number would be of the order of $20^{4/3}$ or about 50.

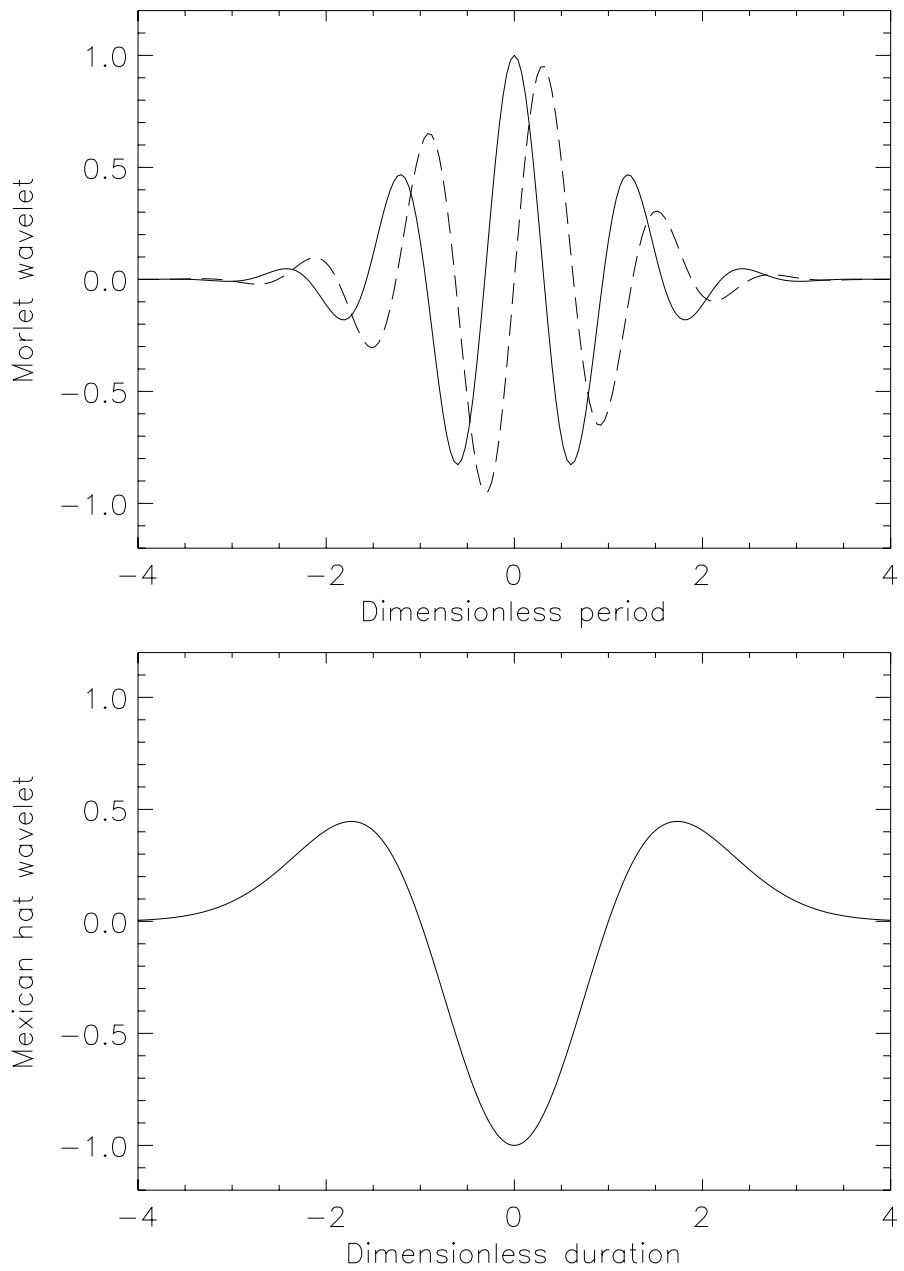


Figure 22: *Top:* Real (solid line) and imaginary (dashed line) parts of the Morlet wavelet for $z_0 = 5$. *Bottom:* The Mexican hat wavelet.

Just as in the case of the Fourier power spectrum, the temporal/spectral distribution of energy formulae rest on Parseval's theorem [2],

$$\int_{-\infty}^{\infty} |u(t)|^2 dt = \frac{1}{c_g} \int_0^{\infty} d\kappa \int_{-\infty}^{\infty} dt |u_g(\kappa, t)|^2 = \int_0^{\infty} 2E_{Mo,Mx}(\kappa) d\kappa, \quad (45)$$

by which the expression $|u_2(\kappa, t)|^2/2c_g$ can be interpreted as the *local* energy spectral density. E_{Mo} and E_{Mx} are the Morlet and Mexhat wavelet alternatives to E_F describing the spectral distribution of energy⁴.

Spectral decomposition of the Reynolds stress can also be achieved with Mexhat wavelets: it was shown in [9] that a simple inverse transform formula holds:

$$u(t) = \int_0^{\infty} U_2(\kappa, t) d\kappa, \quad (46)$$

where

$$U_2(\kappa, t) = \pi^{-1/2} 2^{-7/4} \kappa^{-1/2} u_4(\kappa/\sqrt{2}, t). \quad (47)$$

Here u_4 is the wavelet transform of u by the wavelet $g_4(t) = d^2(g_2(t))/dt^2$. Now consider the $u - v$ -correlation. Using Eq.(46), it can be rewritten in the form [10]

$$\begin{aligned} -\bar{uv} &= - \int_{-\infty}^{\infty} \int_{-\infty}^{\infty} \overline{U_2(\kappa_u, t)} V_2(\kappa_v, t) \kappa_u \kappa_v d(\log \kappa_u) d(\log \kappa_v) \\ &= \int_{-\infty}^{\infty} \int_{-\infty}^{\infty} \kappa_u \kappa_v R_{Mx}(\kappa_u, \kappa_v) d(\log \kappa_u) d(\log \kappa_v). \end{aligned} \quad (48)$$

Therefore, the Reynolds stress can be decomposed into contributions from the plane of the logarithms of durations of each component signal. A diagonal section ($\kappa_u = \kappa_v$) is used in the next sections.

⁴For the Mexhat wavelet, the relationship between the Fourier frequency f and the inverse wavelet duration κ^{-1} was established [8] as $f/\kappa = \sqrt{2.5}/2\pi = .2516$, or approximately 4 wavelet durations per period of the corresponding sine wave. This relation is used to plot the wavelet power spectra in all figures below in terms of conventional frequency instead of wavelet duration scales.

Note that the Morlet wavelet is defined in this report with a unit frequency of the oscillation rather than of the envelope, so that no further conversion is required.

REPORT DOCUMENTATION PAGE			<i>Form Approved OMB No. 0704-0188</i>
Public reporting burden for this collection of information is estimated to average 1 hour per response, including the time for reviewing instructions, searching existing data sources, gathering and maintaining the data needed, and completing and reviewing the collection of information. Send comments regarding this burden estimate or any other aspect of this collection of information, including suggestions for reducing this burden, to Washington Headquarters Services, Directorate for Information Operations and Reports, 1215 Jefferson Davis Highway, Suite 1204, Arlington, VA 22202-4302, and to the Office of Management and Budget, Paperwork Reduction Project (0704-0188), Washington, DC 20503.			
1. AGENCY USE ONLY (Leave blank)	2. REPORT DATE	3. REPORT TYPE AND DATES COVERED	
	February 2004	Technical Memorandum	
4. TITLE AND SUBTITLE		5. FUNDING NUMBERS	
Estimation of Time Scales in Unsteady Flows in a Turbomachinery Rig		WU-22-522-31-23	
6. AUTHOR(S)			
Jacques Lewalle and David E. Ashpis			
7. PERFORMING ORGANIZATION NAME(S) AND ADDRESS(ES)		8. PERFORMING ORGANIZATION REPORT NUMBER	
National Aeronautics and Space Administration John H. Glenn Research Center at Lewis Field Cleveland, Ohio 44135-3191		E-14350	
9. SPONSORING/MONITORING AGENCY NAME(S) AND ADDRESS(ES)		10. SPONSORING/MONITORING AGENCY REPORT NUMBER	
National Aeronautics and Space Administration Washington, DC 20546-0001		NASA TM—2004-209452	
11. SUPPLEMENTARY NOTES			
Jacques Lewalle, Syracuse University, Department of Mechanical, Aerospace, and Manufacturing Engineering, Syracuse, New York 13244; and David E. Ashpis, NASA Glenn Research Center. Responsible person, David E. Ashpis, organization code 5820, 216-433-8317, E-mail: Ashpis@nasa.gov.			
12a. DISTRIBUTION/AVAILABILITY STATEMENT		12b. DISTRIBUTION CODE	
Unclassified - Unlimited Subject Categories: 02, 07, and 34		Distribution: Nonstandard	
Available electronically at http://gltrs.grc.nasa.gov This publication is available from the NASA Center for AeroSpace Information, 301-621-0390.			
13. ABSTRACT (<i>Maximum 200 words</i>)			
Time scales in turbulent and transitional flow provide a link between experimental data and modeling, both in terms of physical content and for quantitative assessment. The problem of interest here is the definition of time scales in an unsteady flow. Using representative samples of data from GEAE low pressure turbine experiment in low speed research turbine facility with wake-induced transition, we document several methods to extract dominant frequencies, and compare the results. We show that conventional methods of time scale evaluation (based on autocorrelation functions and on Fourier spectra) and wavelet-based methods provide similar information when applied to stationary signals. We also show the greater flexibility of the wavelet-based methods when dealing with intermittent or strongly modulated data, as are encountered in transitioning boundary layers and in flows with unsteady forcing associated with wake passing. We define phase-averaged dominant frequencies that characterize the turbulence associated with freestream conditions and with the passing wakes downstream of a rotor. The relevance of these results for modeling is discussed in the paper.			
14. SUBJECT TERMS		15. NUMBER OF PAGES	
Wavelets; Turbulence; Turbomachinery; Unsteady flow; Transition; Wakes; Boundary layer		47	
		16. PRICE CODE	
17. SECURITY CLASSIFICATION OF REPORT	18. SECURITY CLASSIFICATION OF THIS PAGE	19. SECURITY CLASSIFICATION OF ABSTRACT	20. LIMITATION OF ABSTRACT
Unclassified	Unclassified	Unclassified	